US Department
of Transportation

**Federal Railroad
Administration**

Evaluation of Semi-Empirical Analyses for Tank Car Puncture Velocity, Part II: Correlations with Engineering Analyses

Office of Research and
Development
Washington, DC 20590

D.Y. Jeong
Y.H. Tang
A.B. Perlman

U.S. Department of Transportation
Research and Special Programs Administration
Volpe National Transportation Systems Center
Cambridge, Massachusetts 02142-1093

DOT/FRA/ORD-01/21.II

Final Report
November 2001

REPORT DOCUMENTATION PAGE

Form Approved
OMB No. 0704-0188

1. AGENCY USE ONLY (Leave blank)	2. REPORT DATE	3. REPORT TYPE & DATES COVERED
	November 2001	Final Report –August 1998

4. TITLE AND SUBTITLE
Evaluation of Semi-Empirical Analyses for Railroad Tank Car Puncture Velocity, Part II: Correlations with Engineering Analyses

5. FUNDING NUMBERS
R-9002/RR-928

6. AUTHOR(S)
D.Y. Jeong, Y.H. Tang, and A.B. Perlman

7. PERFORMING ORGANIZATION NAME(S) AND ADDRESS(ES)
U.S. Department of Transportation
Research and Special Programs Administration
Volpe National Transportation Systems Center
Cambridge, MA 02142-1093

8. PERFORMING ORGANIZATION REPORT NUMBER
DOT-VNTSC-FRA-99-10

9. SPONSORING/MONITORING AGENCY NAME(S) AND ADDRESS(ES)
Federal Railroad Administration
Office of Research and Development
1120 Vermont Ave., NW MS20
Washington, D.C. 20590

10. SPONSORING OR MONITORING AGENCY REPORT NUMBER
DOT/FRA/ORD-01/21.II

11. SUPPLEMENTARY NOTES

12a. DISTRIBUTION/AVAILABILITY
This document is available to the U.S. public through the National technical Information Service, Springfield, VA 22161. This document is also available on the FRA web site at www.fra.dot.gov.

12b. DISTRIBUTION CODE

13. ABSTRACT (Maximum 200 words)
This report is the second in a series focusing on methods to determine the puncture velocity of railroad tank car shells. In this context, puncture velocity refers to the impact velocity at which a coupler will completely pierce the shell and puncture the tank.

In the first report in this series, a set of semi-empirical equations was evaluated by comparing calculated puncture velocities with data from tank car impact tests. These equations were originally developed by the RPI-AAR Tank Car Safety Committee and later modified by the industry to account for head shield protection and jacket insulation. The semi-empirical equations generally produced reasonable and conservative estimates of puncture velocity when compared with the experimental data. However, differences between the calculated and observed results become more widespread when the tank is pressurized or when shield protection is present. Moreover, alternative methods to determine puncture velocity may be observed by the industry to avoid over-design.

In this report, methods to predict puncture velocity based only on engineering mechanics principles (i.e., no empiricism) are developed and described. Results from the semi-empirical approach are compared with results from the engineering methods. These methods rely on both analytical and computational tools to examine the structural behavior of tanks with ellipsoidal shapes. These tools include finite element and dynamic lumped mass models.

14. SUBJECT TERMS
tank car coupler impact, finite-element analysis, indentation, puncture velocity, tank car head shield protection

15. NUMBER OF PAGES
68

16. PRICE CODE

17. SECURITY CLASSIFICATION OF REPORT	18. SECURITY CLASSIFICATION OF THIS PAGE	19. SECURITY CLASSIFICATION OF ABSTRACT	20. LIMITATION OF ABSTRACT
Unclassified	Unclassified	Unclassified	

PREFACE

The work described in this report was performed by the John A. Volpe National Transportation Systems Center (Volpe Center) as part of a research program to develop technical information and criteria for evaluating the structural integrity of railroad tank cars. This research is being conducted in support of the Equipment and Operating Practices Research Division of the Office of Research and Development of the Federal Railroad Administration (FRA). The FRA program manager for tank car safety research is Mr. Jose Pẽna.

This report is the second in a series focusing on the puncture resistance of tank car shells from the impact of couplers from other cars, broken rails, and other objects. The first report in this series described a semi-empirical approach to calculate the puncture velocity, defined as the impact velocity that will cause full penetration of the impacting object into the tank. The semi-empirical approach was evaluated by comparing calculated puncture velocities with data obtained from impact tests conducted on full-scale and actual tank cars. The semi-empirical approach generally produced reasonable but conservative estimates of puncture velocity. Alternative methods may be needed by the industry to avoid over-design.

In this report, methods based on engineering mechanics principles (i.e., no empiricism) are described to determine the puncture velocity of tank car shells. Both analytical and computational methods are used in the engineering methodologies. The analytical model examines the crushing behavior of a rigid-plastic ellipsoidal shell. Computational methods are carried out with finite element models. Dynamic lumped-mass models are also developed to relate applied force to impact velocity.

METRIC/ENGLISH CONVERSION FACTORS

ENGLISH TO METRIC	METRIC TO ENGLISH
LENGTH (APPROXIMATE)	**LENGTH (APPROXIMATE)**
1 inch (in) = 2.5 centimeters (cm)	1 millimeter (mm) = 0.04 inch (in)
1 foot (ft) = 30 centimeters (cm)	1 centimeter (cm) = 0.4 inch (in)
1 yard (yd) = 0.9 meter (m)	1 meter (m) = 3.3 feet (ft)
1 mile (mi) = 1.6 kilometers (km)	1 meter (m) = 1.1 yards (yd)
	1 kilometer (km) = 0.6 mile (mi)
AREA (APPROXIMATE)	**AREA (APPROXIMATE)**
1 square inch (sq in, in^2) = 6.5 square centimeters (cm^2)	1 square centimeter (cm^2) = 0.16 square inch (sq in, in^2)
1 square foot (sq ft, ft^2) = 0.09 square meter (m^2)	1 square meter (m^2) = 1.2 square yards (sq yd, yd^2)
1 square yard (sq yd, yd^2) = 0.8 square meter (m^2)	1 square kilometer (km^2) = 0.4 square mile (sq mi, mi^2)
1 square mile (sq mi, mi^2) = 2.6 square kilometers (km^2)	10,000 square meters (m^2) = 1 hectare (ha) = 2.5 acres
1 acre = 0.4 hectare (he) = 4,000 square meters (m^2)	
MASS - WEIGHT (APPROXIMATE)	**MASS - WEIGHT (APPROXIMATE)**
1 ounce (oz) = 28 grams (gm)	1 gram (gm) = 0.036 ounce (oz)
1 pound (lb) = 0.45 kilogram (kg)	1 kilogram (kg) = 2.2 pounds (lb)
1 short ton = 2,000 pounds (lb) = 0.9 tonne (t)	1 tonne (t) = 1,000 kilograms (kg)
	= 1.1 short tons
VOLUME (APPROXIMATE)	**VOLUME (APPROXIMATE)**
1 teaspoon (tsp) = 5 milliliters (ml)	1 milliliter (ml) = 0.03 fluid ounce (fl oz)
1 tablespoon (tbsp) = 15 milliliters (ml)	1 liter (l) = 2.1 pints (pt)
1 fluid ounce (fl oz) = 30 milliliters (ml)	1 liter (l) = 1.06 quarts (qt)
1 cup (c) = 0.24 liter (l)	1 liter (l) = 0.26 gallon (gal)
1 pint (pt) = 0.47 liter (l)	
1 quart (qt) = 0.96 liter (l)	
1 gallon (gal) = 3.8 liters (l)	
1 cubic foot (cu ft, ft^3) = 0.03 cubic meter (m^3)	1 cubic meter (m^3) = 36 cubic feet (cu ft, ft^3)
1 cubic yard (cu yd, yd^3) = 0.76 cubic meter (m^3)	1 cubic meter (m^3) = 1.3 cubic yards (cu yd, yd^3)
TEMPERATURE (EXACT)	**TEMPERATURE (EXACT)**
[(x-32)(5/9)] °F = y °C	[(9/5) y + 32] °C = x °F

QUICK INCH - CENTIMETER LENGTH CONVERSION

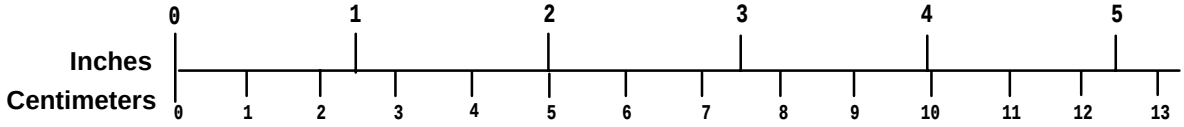

QUICK FAHRENHEIT - CELSIUS TEMPERATURE CONVERSION

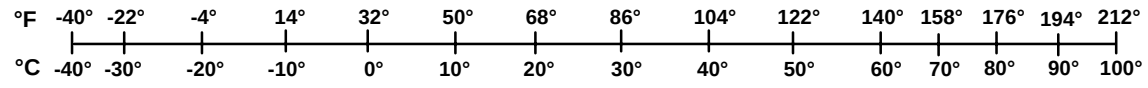

For more exact and or other conversion factors, see NIST Miscellaneous Publication 286, Units of Weights and Measures. Price $2.50 SD Catalog No. C13 10286

Updated 6/17/98

TABLE OF CONTENTS

LIST OF FIGURES

Figure **Page**

LIST OF FIGURES (continued)

Figure **Page**

LIST OF TABLES

LIST OF ABBREVIATIONS AND SYMBOLS

AAR	Association of American Railroads
FRA	Federal Railroad Administration
RPI	Railway Progress Institute
RSPA	Research and Special Programs Administration

a	tank head radius
b	ellipsoidal shell depth
b/a	aspect ratio
d	indentation
g	acceleration due to gravity (386 in/s^2)
h	plate or shell thickness
h_{eff}	effective thickness
h_h	head thickness
h_j	jacket thickness
h_s	shield thickness
k	spring constant
m_1	ram car mass
m_2	reaction car mass
m_{eff}	effective mass
n	exponent in Ramberg-Osgood equation
p	internal pressure
r	radial distance
t	time
v	velocity
v_o	initial impact velocity
v_p	puncture velocity
w_o	plate or shell deflection
$\dot{w}$	deflection rate
x, y, z	Cartesian coordinates
A	constant
B	constant
C	constant
E	Young's modulus or modulus of elasticity
$\dot{E}$	dissipation energy
E_{tan}	tangent modulus
F	coupler force
K	constant in Ramberg-Osgood equation
K_G	gap factor
M_o	fully-plastic moment
P	applied load

LIST OF ABBREVIATIONS AND SYMBOLS (continued)

P_o	dimensionless pressure parameter
R	radial distance to define location of plastic hinge circle
W_1	ram car weight
W_2	reaction car weight
α	ratio of reaction car weight to ram car weight
ε	strain
ε_f	failure strain
ε_{max}	maximum strain
ε_p	effective plastic strain
θ	angular coordinate to define location of plastic hinge circle
δ	deflection
Δ	gap distance between head shield and tank head
λ	dimensionless internal pressure parameter
ν	Poisson's ratio
ρ	radius of curvature
σ	stress
σ_o	flow stress
σ_{YLD}	yield strength
σ_{ULT}	ultimate tensile strength
τ	shear stress
τ_{rz}	transverse shear stress
τ_u	ultimate shear strength
ω	natural frequency

EXECUTIVE SUMMARY

This report describes engineering methods to determine the puncture velocity of tank cars. In this context, the puncture velocity is defined as the velocity at which puncture may be expected to occur.

Prior to the work described in this report, puncture velocity of railroad tank cars has been calculated by the industry with the aid of semi-empirical equations. These semi-empirical equations were originally developed by the Railway Progress Institute - Association of American Railroads (RPI-AAR) Tank Car Safety Research and Test Project, and were later modified by the industry to include the effect of head shield protection and jacket insulation. The semi-empirical approach to calculate puncture velocity was evaluated in a previous technical report by comparing calculations with experimental data from various sources.

In this report, methods are developed to determine puncture velocity based on engineering mechanics principles. That is, no empiricism has been incorporated into the analyses. These analyses include a rigid-plastic ellipsoidal shell model, finite element models, and dynamic lumped-mass modeling.

The rigid-plastic ellipsoidal shell model and the finite element analyses indicate that the magnitude of the indentation due to impact depends strongly on the shape and depth of the tank car head (i.e., aspect ratio of the ellipsoid). Sensitivity studies also reveal that load-deflection behavior of the shell is strongly affected by material properties such as yield strength. Shell thickness, internal pressure, and off-center loading were found to have a moderate effect on indentation. Tank diameter had a weak influence on the load versus deflection behavior.

Results from the engineering models are in good agreement with those from the semi-empirical equations for six cases examining the puncture velocity of non-pressurized, bare head tanks. The finite element calculations were less than the semi-empirical results in all cases with 2 percent outage, while the semi-empirical results were less than the finite element (FE) results in all cases with 100 percent outage. Further examination of the tests data suggests that the presence of liquid inside the tank (outage) has a stiffening effect on indentation.

Both the effect of liquid inside the tank and the effect of tank car head protection (such as a head shield or jacket) should be addressed in future work.

1. INTRODUCTION

Each year the nation's railroad tank cars make about one million shipments with hazardous materials. These materials can be poisonous, corrosive, flammable or pose other health or safety hazards. Approximately 1,000 accidental releases of hazardous materials from tank cars are reported annually to the U.S. Department of Transportation (DOT), Research and Special Programs Administration (RSPA), Office of Hazard Materials Safety. Most are small spills and leaks but some lead to injuries, property damage, environmental contamination and other consequences of concern.

Two DOT agencies - the Federal Railroad Administration (FRA) and the Research and Special Programs Administration (RSPA) - share responsibility for tank car safety in the United States. Moreover, these agencies determine which materials must be shipped in tank cars best designed to withstand train crashes and to prevent accidental spills of hazardous materials. In recent years, both the FRA and the railroad industry, through the Railway Progress Institute - Association of American Railroads (RPI-AAR) Tank Car Safety Research and Test Project, have worked cooperatively to develop standards for shipment of hazardous materials in tank cars. These efforts have improved the safety of tank car operations.

From 1978 to 1984 regulations were changed to require head protection on most pressure cars carrying flammable gases and certain other hazardous materials. The purpose of head protection is to increase the resistance of the tank head to puncture from the couplers of other rail cars, broken rails, and other objects. The current regulations, however, do not prescribe how this head protection performance standard must be met but permit, as an option, the use of steel plates mounted in front of the tank heads which act as head shield protection. The industry has now requested a performance standard for head protection based on the ability to predict puncture velocity in lieu of actual testing.

Studies on tank car puncture were conducted by the RPI-AAR Tank Car Safety Research and Test Project in the 1970s. Data were collected during impact tests on structures of varying scales. As part of that study, empirical equations were developed to calculate the velocity at which the tank car shell would puncture (referred to as the puncture velocity). More recently, the DuPont Company modified the semi-empirical equations to include the effect of head protection and jacket insulation for inter-modal tanks (Belport, 1993). Subsequently, the FRA requested technical support from the Volpe National Transportation Systems Center (Volpe Center) to evaluate the applicability of the semi-empirical equations to actual tank cars.

This report is the second in a series describing methods to calculate the puncture velocity of tank car shells. In the first report, the industry's semi-empirical approach to determine puncture velocity was evaluated by comparing predictions with data from tank car impact tests (Jeong, et al., 2001). Sixty-five test cases involving full-scale and actual tank cars were considered. The data were obtained from three different sources (Phillips and Olsen, 1972; Larson, 1992; and Coltman and Hazel, 1992). In general, the semi-empirical approach underestimated the actual

puncture velocity indicating that the approach tends to be conservative. As such, alternative methods may be preferred to avoid over-design.

In this report, methods based on engineering mechanics principles are developed and described. No empiricism has been incorporated into the methods presented here. Analytical and computational methods are applied to develop structural models of tank car heads. In these models, the tank car head is represented as an ellipsoidal shell. Specifically, the analytical method is a model that examines crushing of rotationally symmetric rigid plastic shells. Rotational symmetry implies that the shell is loaded at its center. The assumptions of rigid plastic material behavior and rotational symmetry allow for the derivation of analytical expressions for the load deflection response of the shell. The finite element method is used to examine the more general case of off-center loading and elastic-plastic material behavior. A dynamic lumped-mass model is also developed to relate impact velocity to the force applied to the tank head. Finally, appropriate failure criteria are examined to estimate when puncture of the tank will occur.

2. SEMI-EMPIRICAL ANALYSES TO CALCULATE PUNCTURE VELOCITY

The semi-empirical equations to calculate puncture velocity were evaluated in a previous report by comparing predictions with experimental data (Jeong, et al., 2001). These equations were originally developed by the RPI-AAR Tank Car Safety Project for bare tank car heads (Shang and Everett, 1972), and later modified by the DuPont Company to account for head shield protection and jacket insulation in inter-modal tanks. The calculations of puncture velocity based on these equations were within reasonable agreement with the available experimental data. However, differences between the calculated and observed results became more widespread when the tanks were pressurized or when head shield protection was present.

The semi-empirical equations are briefly summarized in this section for reference purposes.

(1) Maximum impact force as a function of indentation.
The maximum force due to a coupler impacting the head of a tank is related to the indentation or dent size by the following equation:

$$F(d) = 35\times 10^{6} d^{3/2}\left(\frac{h}{2a}\right)^{3}\left(\frac{p+15}{15}\right)^{0.6} \tag{1}$$

where F is the maximum impact force (in units of kips), d is the indentation (in inches), h is the shell thickness (in inch), a is the radius of the tank head (in inches), and p is the internal pressure (in psi). The exponent of 3/2 for d indicates that a Hertzian relationship between the contact force and the indentation was assumed in the formulation. The Hertz contact assumption implies that the problems of elastic contact and elastic impact are treated identically in this formulation. The assumption of Hertz contact may be valid for low-velocity impacts, but may be questionable for impacts resulting in puncture or other types of failure.

(2) Indentation as a function of impact velocity.
The semi-empirical equation for indentation or dent size is a linear function of impact velocity:

$$d(v) = 8.8\times 10^{-5}\left(\frac{2a}{h}\right)^{2} \alpha^{1/16}\left(\frac{W_1 v}{g}\right)\left[1-0.23\left(\frac{p}{40}\right)^{0.5}\right] \tag{2}$$

where v is the impact velocity (in miles per hour), W_1 is the weight of the impacting car (in kips), and g is the acceleration due to gravity (386 in/s^2). Also, α is the ratio between the weights of the tank car and the ram car or W_2/W_1.

(3) Failure criterion.

Failure is assumed to occur when the maximum stress exceeds or is equal to the ultimate shear strength. For this purpose, the transverse shear component of stress is calculated for a flat circular plate subjected to a concentrated load offset from the center to represent a "knuckle" impact. An infinite series solution for this configuration is available in the open literature (for example, refer to page 290 of Timoshenko and Woinowsky-Krieger, 1959). The RPI-AAR formulation is based upon the first five terms of the infinite series solution which gives:

$$t = 1.81\frac{F}{ah} \tag{3}$$

where F is the coupler force and a is the radius of the circular plate. Mathematically, the failure criterion can be expressed as:

$$1.81\frac{F}{ah} \geq t_u \tag{4}$$

where t_u is the ultimate shear strength of the head material. In general, mechanical properties for a given material are reported in terms of yield strength, ultimate tensile strength, and percent elongation. Assuming that triaxial stresses are related to uniaxial test data by the von Mises equivalent stress, the ultimate shear strength is equal to 57.7percent of the ultimate tensile strength.

2.1 Puncture Velocity for a Bare Tank Car Head

An equation to calculate the maximum coupler force as a function of impact velocity can be derived by combining equations (1) and (2):

$$F(v) = 0.00383a^{3/32}(W_1 v)^{3/2}\, l\,(p) \tag{5}$$

where $l\,(p)$ is a dimensionless function of internal pressure defined as:

$$l\,(p) = \left[1 - 0.23\left(\frac{p}{40}\right)^{0.5}\right]^{3/2}\left(\frac{p+15}{15}\right)^{0.6} \tag{6}$$

The numerical value of l is always greater than or equal to one. For example, a value of 1.0 corresponds to the case of no internal pressure; a value of 1.72 to a pressure of 100 psi.

An expression to calculate the puncture velocity (i.e., the velocity at which puncture of the tank may be expected) can be derived by substituting the equation for maximum coupler force into the failure criterion. In other words, combining equations (4) and (5), and then solving for the velocity gives:

$$v_p = \frac{27.6}{W_1 a^{1/16}} \left[\frac{t_u a h}{l(p)} \right]^{2/3} \tag{7}$$

In this equation, v_p is the puncture velocity in miles per hour (mph).

2.2 Puncture Velocity for a Tank Car Head with Head Shield and/or Jacket

In the case of head shield protection and/or jacket insulation, the semi-empirical equations include three auxiliary parameters. The first of these parameters is referred to as the effective thickness, defined by:

$$h_{eff} = \left[h_h^{1.33} + h_s^{1.33} + h_j^{1.33} \right]^{1/1.33} \tag{8}$$

where h_h is the tank car head thickness, h_s is the head shield thickness, and h_j is the jacket thickness. The exponent of 1.33 is an empirical constant. Another auxiliary parameter is referred to as the gap factor:

$$K_G = \frac{1}{\sqrt{1 - \dfrac{2F(v_{pb}) \cdot \Delta \cdot g}{(17.6 v_{pb})^2 W_1}}} \tag{9}$$

where D is the gap or distance between the head shield and the tank shell and g is the acceleration due to gravity (386 in/s^2). The conversion factor of 17.6 in/s = 1 mph has also been included in this equation. In addition, F is the maximum coupler force calculated from equation (5) for a velocity v_{pb} which is the puncture velocity for a bare tank car head (in mph) with effective thickness and is defined as:

$$v_{pb} = \frac{27.6}{W_1 a^{1/16}} \left[\frac{t_u \cdot a \cdot h_{eff}}{l(p)} \right]^{2/3} \tag{10}$$

Then, the puncture velocity for a tank car head with head shield protection and/or jacket insulation can be calculated from:

$$v_p = K_G \cdot v_{pb} \tag{11}$$

where K_G is the gap factor defined by equation (9) and v_{pb} is defined by equation (10).

2.3 Discussion of Semi-Empirical Approach

The semi-empirical approach to calculate the puncture velocity of tank cars is appealing because of its simplicity. As such, the semi-empirical approach was evaluated in a previous report by comparing predictions with results from impact tests conducted on full-scale and actual tank cars (Jeong, et al., 2001). The comparisons indicate that the semi-empirical equations provide reasonable but conservative estimates of puncture velocity. The conservatism may stem from its simplicity.

Further review of the semi-empirical approach indicates that the following factors have not been taken into account explicitly:

amount of liquid in the tank (outage) and
geometry of the tank car head (shape and depth of the tank car head).

The effect of outage can be demonstrated from an examination of the available impact test data involving non-pressurized tanks. For example, Table 1 lists forces and indentations measured during ten impact tests on bare tank car heads with varying combinations of tank diameter, shell thickness, and outage. In order to minimize the effects from variations in tank diameter and shell thickness, the data were normalized using the following procedure. The measured indentation, w_o, is divided by the shell thickness, h. The corresponding dimensionless parameter for measured impact force is defined as Pa^2/Eh^4 where P is the measured impact force, a is the radius of the tank, E is the modulus of elasticity (assumed to be 3×10^7 psi for tank car steel), and h is the shell thickness. The normalized data are plotted in Figure 1 which also shows regression curves for the 2 percent outage and 100 percent outage data. The open symbols in the figure represent cases where the outage in the tank was 100 percent (completely empty tanks). Conversely, solid symbols in Figure 1 represent cases for 2 percent outage (almost full). From this normalization procedure, Figure 1 suggests that the presence of liquid in the tank has a stiffening effect on the load deflection behavior of bare tank car heads.

The effect of the tank car head geometry (shape and depth of the tank car head) will be demonstrated through structural analyses of curved shells. These analyses are described in the next section of this report.

Table 1. Data from Impact Tests on Bare Tank Car Heads

Case No.	Outage	Reaction Car Weight W_2 (kips)	Tank Diameter 2a (inches)	Shell Thickness h (inch)	Measured Impact Force (kips)	Measured Indentation (inches)
1	2%	96.6	78	0.500	55	2.75
					381	12
2	100%	48.5	87.5	0.500	59	6.5
					126	13.25
					137	13.5
					208	16
3	2%	107.3	80	0.438	89	6.5
					410	16.5
4	100%	48.0	80	0.438	-	-
5	100%	40.9	83	0.438	118	9
6	2%	128.9	88	0.438	141	11.25

NOTES:
(1) All tests performed with non-pressurized tanks.
(2) No measured data were available for Case 4.
(3) In all cases, the ram car weight is 128.9 kips.

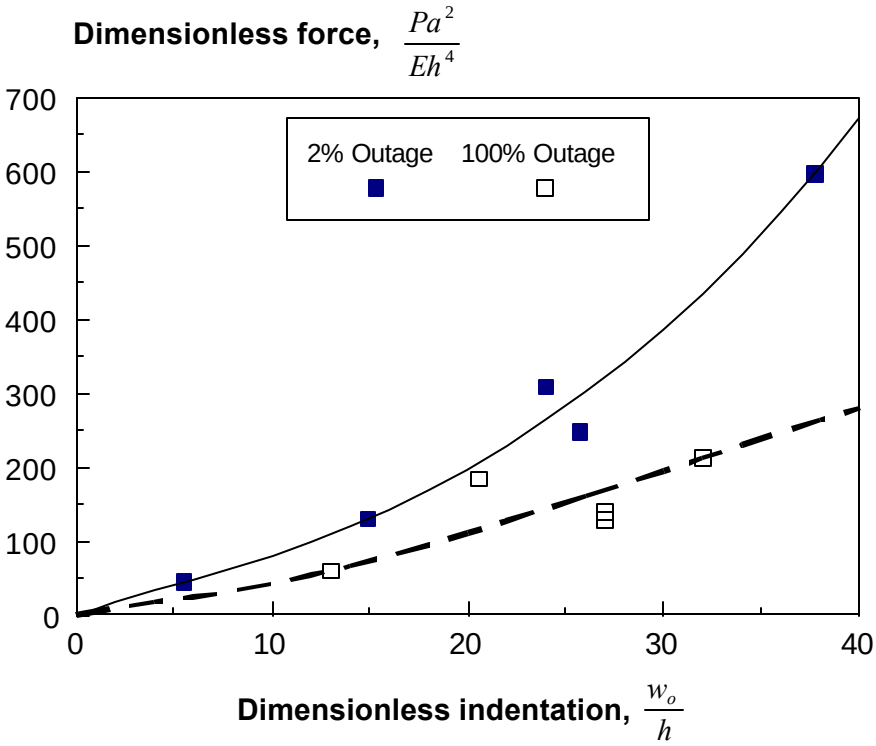

Figure 1. Normalized Impact Data for Bare Tank Car Heads

3. ENGINEERING ANALYSES

In this section, engineering analyses are described that form the basis for rational methods to calculate the puncture velocity of tank cars. These analyses include an analytical model to examine the crushing behavior of an ellipsoidal shell, finite element models of flat plates and curved shells, and dynamic lumped-mass modeling. Moreover, these analyses are developed to determine:

(1) a mechanics-based relation between indentation and impact force,
(2) a mechanics-based relation between impact force and impact velocity, and
(3) a rational criterion for puncture.

3.1 Indentation as a Function of Impact Force

Different models with varying geometries (i.e., flat circular plates versus curved spherical shells) and material behavior (e.g., elastic versus elastic-plastic) were considered to determine the relationship between indentation and impact force.

The semi-empirical equation relating indentation and impact force assumes Hertzian contact which generally applies to contact of linear elastic bodies. For this reason, preliminary calculations for load versus deflection were based on linear-elastic plate theory. Such calculations, however, were found to produce unrealistic deflections. That is, extremely high deflections were calculated for high impact forces (e.g., approximately 100 inches for 2000 kip loads).

3.1.1 Analysis Based on Plastic Collapse

An analytical model was developed previously to calculate the load versus deflection behavior of pressurized hemispherical shells (Lupker, 1990). The model was based on a plastic-collapse model originally developed by de Oliveria and Weirzbicki (1982) for non-pressurized hemispherical shells. In these models, the shell is subjected to a centrally applied concentrated load which results in axisymmetric deformation of the shell. Moreover, assuming both axisymmetric deformation and rigid plastic material behavior provides an analytical expressions for load versus deflection.

In the present study, the analyses developed by de Oliveria and Weirzbicki and by Lupker have been further modified to examine the load deflection behavior of pressurized ellipsoidal shells with an arbitrary aspect ratio. This modification represents a more general case of shell deformation since a hemispherical shell is a special limiting case of an ellipsoidal shell. Referring to Figure 2, the geometry of the ellipsoidal shell is defined by a and b which represent the semi-major axis length of the ellipsoid and semi-minor axis length, respectively. For example, the as-

pect ratio (b/a) for a hemispherical shell is equal to one. In the design of actual tank cars, the aspect ratio is usually less than ½

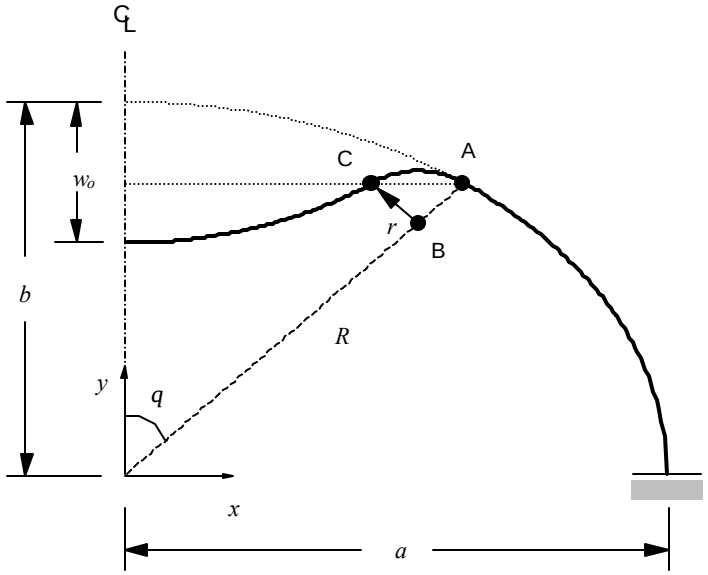

Figure 2. Schematic of Rigid Plastic Deformation of an Ellipsoidal Shell

Expressions for the load and deflection of an ellipsoidal shell are written in terms of a parameter q. Physically, q is the angle at which a plastic-hinge circle forms as a result of the rigid plastic deformation (Figure 2). As the applied load increases and plastic deformation spreads toward the edges of the shell, the angle q increases. The parametric equations for the applied load and center deflection of the shell as functions of the angle q are:

$$F = 2pM_o\left[\frac{4}{3}\frac{r}{h}\left(\frac{b}{a}\right)^2\frac{\sin^2 q}{\cos q}+\frac{R}{r}-1+\frac{4P_o}{ha}\left(R^2-2Rr+\frac{4}{3}r^2\right)\sin^2 q\right] \tag{12}$$

$$w_o = 2\left(1-\frac{r}{R}\right)(b-R\cos q) \tag{13}$$

where M_o is the fully-plastic moment and P_o is a dimensionless pressure parameter which are defined as:

$$M_o = \frac{1}{4}s_o h^2 \qquad\qquad P_o = \frac{pa}{2s_o h} \tag{14}$$

In these equations, s_o is the flow stress, h is the shell thickness, and p is the internal pressure. Also,

$$r = \frac{1}{2\sin\theta}\left(\frac{a}{b}\right)\sqrt{3Rh\cos\theta} \tag{15}$$

$$R = \sqrt{\frac{a^2 b^2}{a^2\cos^2\theta + b^2\sin^2\theta}} \tag{16}$$

The derivation of these equations is given in Appendix A.

Figure 3 shows the effect of flow stress on the load deflection behavior of rigid plastic ellipsoidal shells. These results apply to shells with a tank diameter of 87.5 inches and thickness of ⅛ inch. These dimensions correspond to Case 2 in Table 1 on page 7. Also, the aspect ratio, or ratio of the semi-minor axis length to the semi-major axis length, *b/a,* is assumed to be ¼. The figure indicates that the force level to achieve a given deflection increases as the flow stress increases. An artifact of the rigid plastic assumption is that the force is a finite value when the deflection is zero.[1]

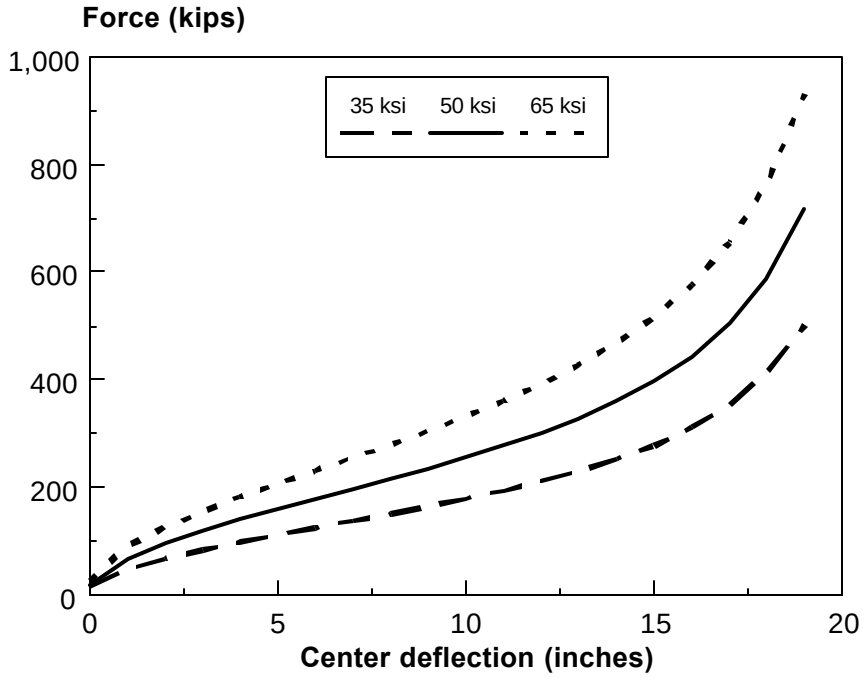

Figure 3. Effect of Flow Stress on Rigid Plastic Analysis of Ellipsoidal Shells

[1] Equation (12) reduces to $F = 2\pi M_o$ when θ is equal to zero which corresponds to the undeformed state.

The effect of the aspect ratio on the load deflection behavior of rigid plastic ellipsoidal shells is shown in Figure 4. These results apply to shells with a tank diameter of 87.5 inches and thickness of ½inch. Also, the flow stress is assumed to be 50 ksi which is equal to the yield strength for AAR TC-128 Grade B tank car steel. These results show that deflection is essentially independent of aspect ratio for force levels below 200 kips. At force levels greater than 200 kips, however, a higher load is needed to achieve a given deflection as the aspect ratio decreases. The effect is magnified as the force levels increase. Moreover, at these higher force levels, the effective stiffness of the shell increases as the aspect ratio decreases.

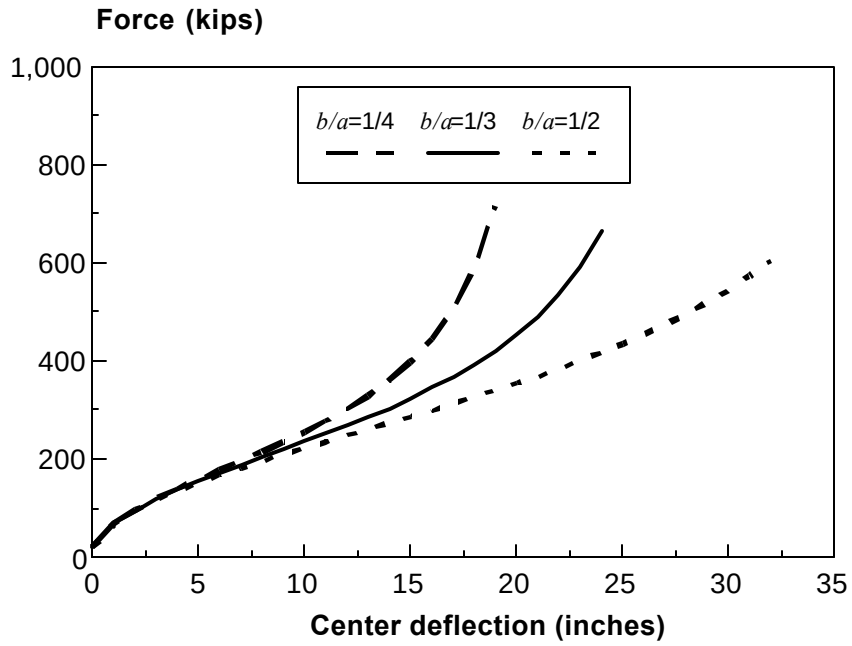

Figure 4. Effect of Aspect Ratio on Rigid Plastic Analysis of Ellipsoidal Shells

The geometry of the tank car head is also defined by the tank diameter and shell thickness. Figure 5 shows the effect of tank diameter on the load deflection behavior of rigid plastic ellipsoidal shells. The values assumed for the tank diameter essentially represent the range of values listed in Table 1 for bare tank car heads. The figure indicates that the load deflection behavior is independent of tank diameter when forces are less than 250 kips. At forces greater than 250 kips, the shell with the larger diameter deflects more at the same force level than the shell with the small diameter. The effect of shell thickness on the load deflection behavior of rigid plastic ellipsoidal shells is shown in Figure 6. This figure indicates that greater force is needed to deflect the thicker shell to the same indentation as the thinner shell. The results in both figures apply to shells with an aspect ratio equal to ¼

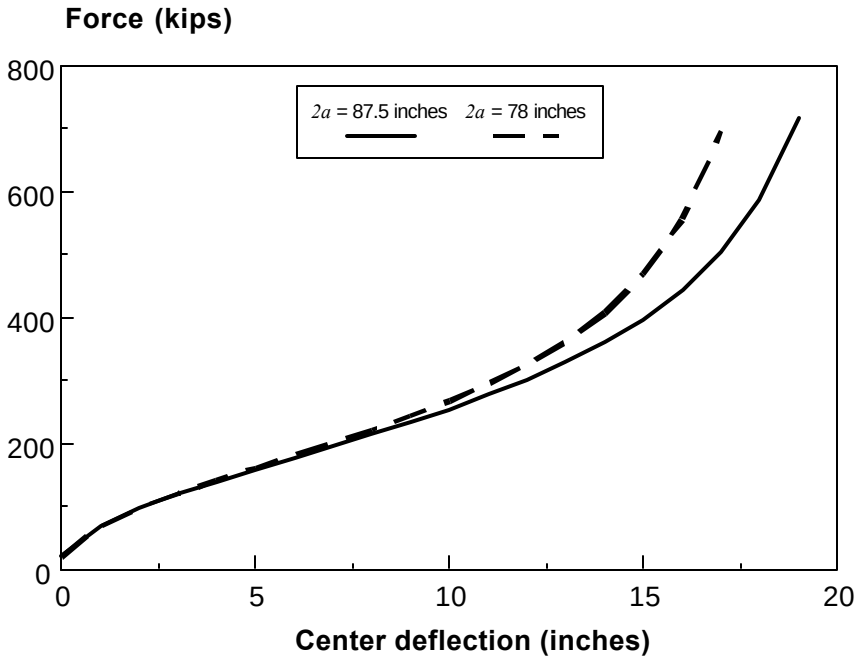

Figure 5. Effect of Tank Diameter on Rigid Plastic Analysis of Ellipsoidal Shells

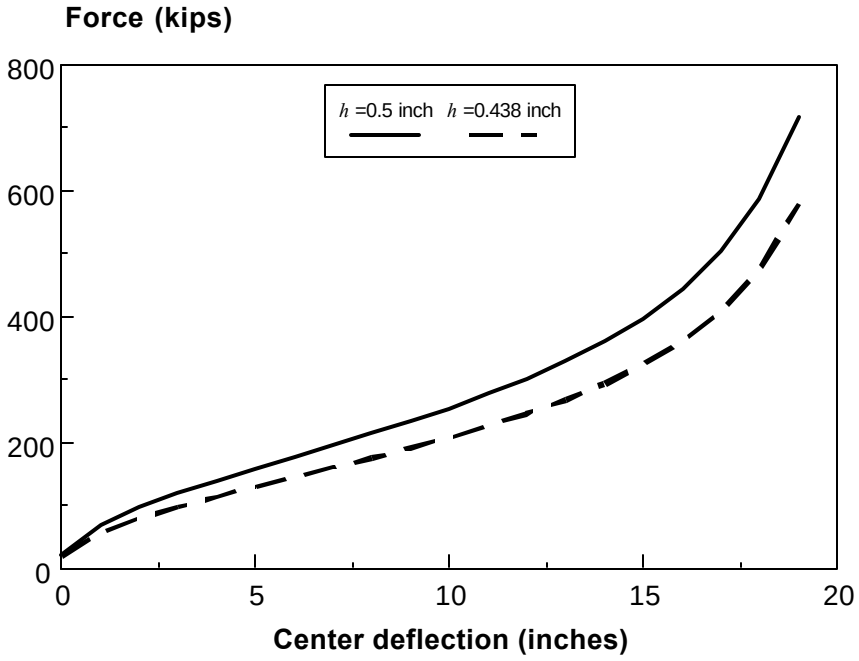

Figure 6. Effect of Shell Thickness on Rigid Plastic Analysis of Ellipsoidal Shells

The effect of internal pressure on the load deflection behavior of rigid plastic shells is shown in Figure 7. These results apply to ellipsoidal shells with an aspect ratio equal to ¼ and a flow

stress equal to 50 ksi. Qualitatively, these results indicate that internal pressure increases the effective stiffness of the shell which is consistent with results from the semi-empirical approach. Quantitatively, however, the effect of internal pressurization as shown in Figure 7 is less than that indicated by the semi-empirical formula for impact force as a function of indentation, as given by equation (1). For example, an internal pressure of 20 psi requires an impact force that is 1.7 times the force for the non-pressurized case to achieve the same indentation according to equation (1). From Figure 7, the same factor is roughly between 1.2 and 1.3. Similarly, an internal pressure of 40 psi requires 2.2 times the force of the non-pressurized case to achieve the same indentation, according to the semi-empirical equation. The same factor is between 1.4 and 1.6, according to the results from the rigid plastic analysis. In other words, the semi-empirical approach estimates a greater effect of internal pressurization on the load deflection response than the rigid plastic ellipsoidal shell model. Tanks are usually pressurized when they contain liquid. Therefore, these comparisons may suggest that the semi-empirical approach overestimates the effect of pressurization to compensate for excluding the effect of outage.

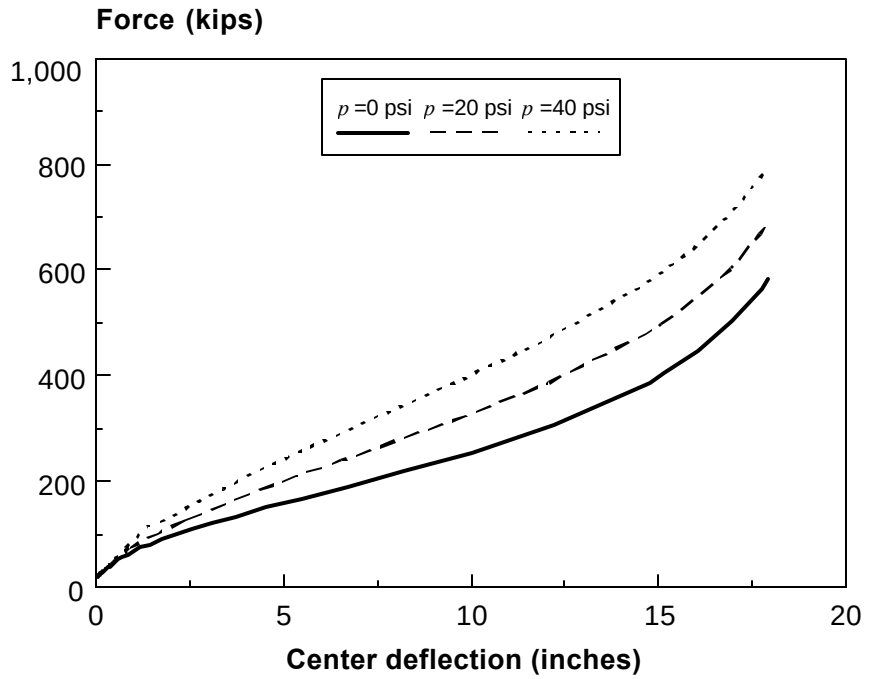

Figure 7. Effect of Internal Pressure on Rigid Plastic Analysis of Ellipsoidal Shells

On one hand, the rigid plastic analysis of ellipsoidal shells is convenient because an analytical solution for load versus deflection is available. On the other hand, the analysis is limited to impacts at the center of the shell. Moreover, the rigid plastic assumption requires knowledge of the flow stress. Conventionally, the flow stress can be taken as the yield strength, the ultimate tensile strength, or the average of the yield and ultimate tensile strengths. However, the results

shown in Figure 3 indicate that the magnitude of the flow stress has a significant influence on the load deflection behavior.
In principle, the limitations of the analytical model for ellipsoidal shells can be handled using the finite element method. That is, the finite element method represents a versatile computational tool that can examine the effects of off-center impacts and more realistic material behavior.

3.1.2 Finite Element Analyses

Finite element (FE) models have been developed by the industry for various purposes, but none seem appropriate for predicting puncture velocity, at this time. In the present study, FE analyses are conducted using the NIKE code for quasi-static loading conditions and the DYNA code for dynamic loading.

The starting point for the finite element analyses in the present study was to approximate the tank car head as a flat circular plate. Various levels of complexity will be incorporated into the finite element modeling after each step has been validated through analytical solutions or available experimental data.

Nonlinear elastic, flat circular plate with clamped edges

The finite element results for a flat circular plate with clamped edges were validated through comparisons with approximate analytical solutions. For example, based on elastic large-deflection plate theory, the relationship between the maximum deflection and total load on the plate is given by (see page 415 of Timoshenko and Woinowsky-Krieger, 1959):

$$\frac{w_o}{h} + A\left(\frac{w_o}{h}\right)^3 = B\frac{Pa^2}{Eh^4} \tag{17}$$

where w_o is the displacement at the center of the plate, h is the plate thickness, a is the radius of the plate, and E is the modulus of elasticity. Also, A and B are constants that depend on the boundary conditions (simply supported versus clamped edges), type of loading (concentrated load versus uniformly distributed load over the entire plate), and Poisson's ratio. Values for A and B are listed in Table 2 for flat circular plates with clamped edges subjected to a concentrated load at the center, and assuming Poisson's ratio is equal to 0.3.

Table 2. Assumed Constants for Large Elastic Deflection Analysis

	A	*B*
Immovable edge	0.443	0.217
Edge free to slide	0.200	0.217

Figure 8 compares the quasi-static finite element (FE) results with the analytical solutions for flat circular plates with movable and immovable edges; i.e., equation (17). These results were conducted for a plate with a diameter of 87.5 inches and a thickness of 0.5 inches. In the finite element model, the total load was distributed uniformly over a square area at the center of the plate. The loaded area was 5 percent of the total surface area of the plate to approximate the application of a concentrated load. The analytical solutions bracket the FE results; the analytical solution for an immovable edge represents the lower bound on the deflection at a given load level while the solution for edges that are free to slide gives the upper bound.

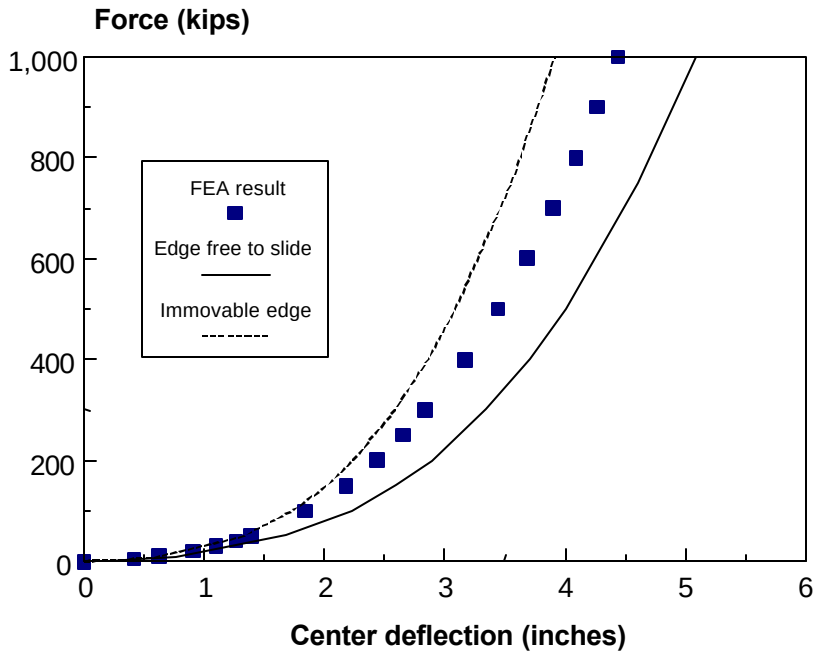

Figure 8. Comparison between Finite Element Analysis and Analytical Solution for Large Elastic Deflection of Flat Circular Plates with Clamped Edges

Elastic-plastic flat circular plate with clamped edges

The next logical progression in the finite element analysis of flat plates is to examine the effect of elastic-plastic material behavior. Elastic-plastic material behavior is represented in the FE models by specifying a stress-strain curve for a given material. Table 3 lists the minimum requirements for AAR TC-128 Grade B tank car steel. These minimum requirements were used to construct a bilinear (i.e., linear hardening) stress-strain curve where the modulus of elasticity E is assumed to be 3×10^7 psi and the tangent modulus E_{tan} is 1.65×10^5 psi (Figure 9).

Table 3. Minimum Requirements for AAR TC-128 Steel

Property	Value
Yield strength, σ_{YLD}	50 ksi
Ultimate tensile strength, σ_{ULT}	81 ksi
Percent elongation	19% in 2 inches

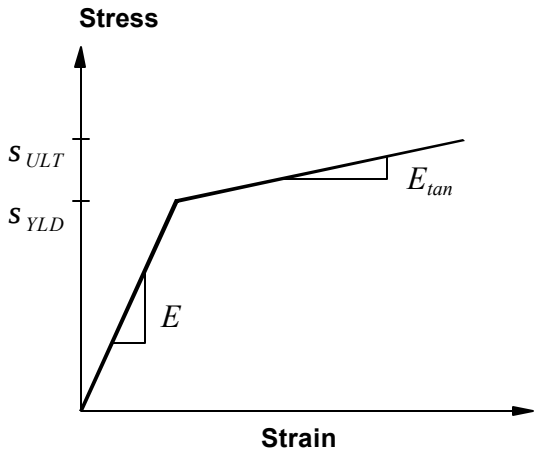

Figure 9. Schematic of Linear-Hardening Stress-Strain Curve

Figure 10 compares the quasi-static finite element results for elastic (with large deflections) versus elastic-plastic material behavior as modeled by the linear strain-hardening stress-strain curve. The results show larger deflections for elastic-plastic plates than for elastic plates under the same load. This result is reasonable because plates that have yielded are less likely to resist deformation. At force levels greater than 200 kips, the relation between load and deflection for the elastic-plastic case is practically linear. The figure also shows a plot of equation (1) for a tank car head with a diameter equal to 87.5 inches and shell thickness equal to 0.5 inch. The load deflection response provided by the analysis of flat plates is much stiffer than the correlated test results.

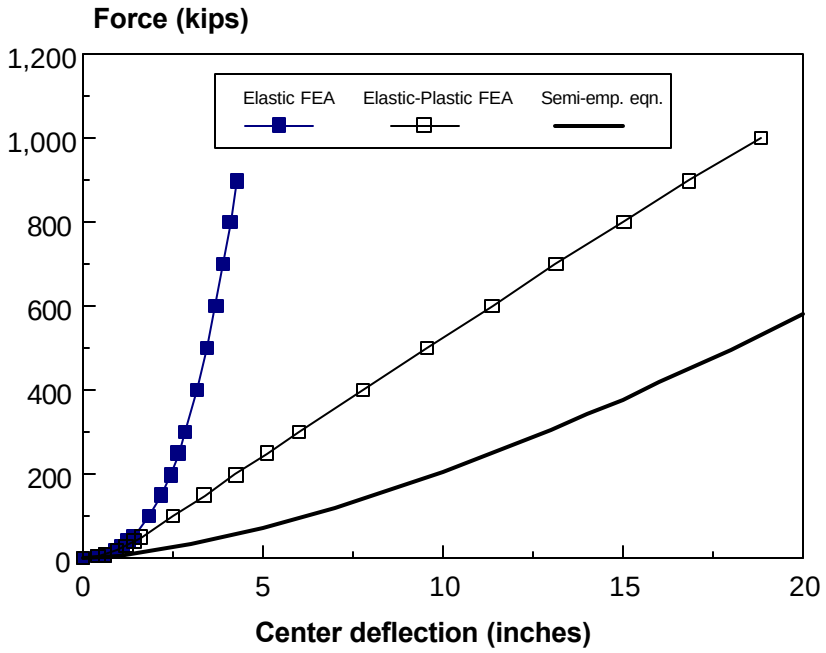

Figure 10. Elastic and Elastic-Plastic Load Deflection Behavior of Flat Circular Plates

Elastic-plastic material behavior may also be modeled using a nonlinear stress-strain curve. For instance, nonlinear strain hardening can be modeled using a Ramberg-Osgood curve which is expressed mathematically as:

$$e = \frac{s}{E} + \left(\frac{s}{K}\right)^n \tag{18}$$

where e is the strain, s is the stress, and E is the modulus of elasticity. Also, K and n are constants, which are equal to 9.68×10^4 ksi and 9.41 respectively for AAR TC-128 steel. Figure 11 compares the linear and nonlinear hardening stress-strain curves used in the finite element analyses. The nonlinear stress-strain curve is effected in the finite element analyses by specifying a piecewise linear relation. The stress-strain relation as modeled by the nonlinear hardening curve provides a smoother transition from the elastic to the plastic stress states, while the linear hardening curve has a discontinuity in slope at the yield strength.

Figure 12 compares the elastic-plastic deformation of flat circular plates with clamped edges as modeled by the linear and nonlinear hardening stress-strain curves. At force levels less than 200 kips, a slightly stiffer load deflection response is evident when the stress-strain curve is approximated by the Ramberg-Osgood equation (nonlinear hardening case). Between 200 and 400 kips, the load deflection behavior is nearly identical. When the forces are greater than 400 kips, the difference in the tangent moduli between the linear and nonlinear hardening models greatly

affects the load deflection response. In other words, the tangent modulus for the linear hardening curve is always greater than the nonlinear hardening case which leads to a stiffer load deflection response.

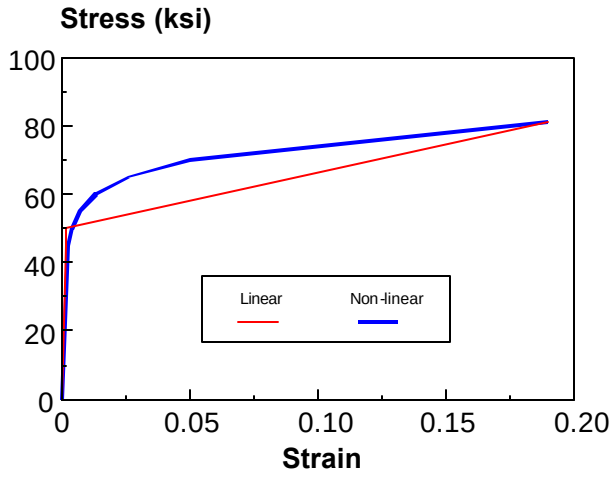

Figure 11. Linear and Nonlinear Hardening Stress-Strain Curves for Tank Car Steel

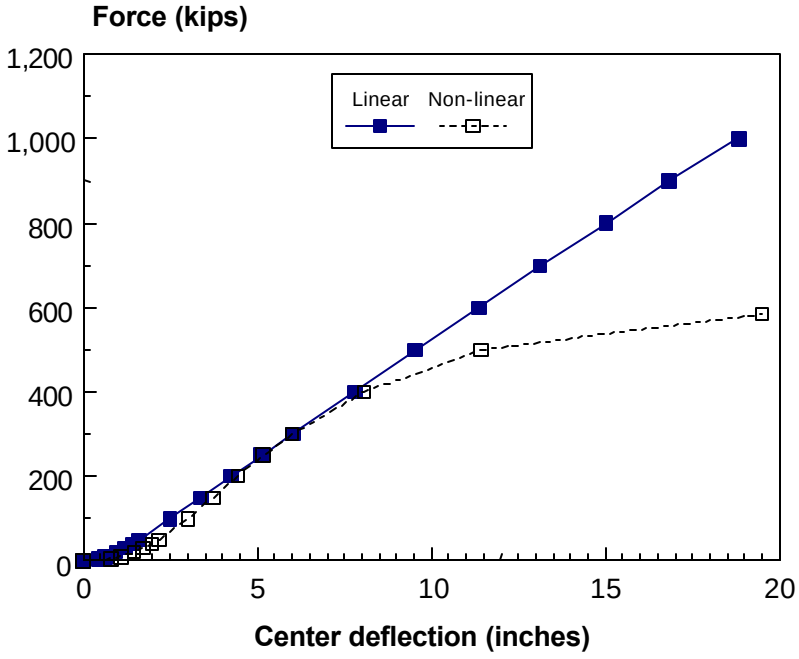

Figure 12. Elastic-Plastic Behavior of Flat Circular Plates Modeled by Linear and Nonlinear Strain Hardening

Elastic-plastic ellipsoidal shells

Since the head of a tank car is actually a curved surface, the next logical step is to vary the geometry of the plate to resemble the head of a tank car. Therefore, hemispherical and ellipsoidal shells are examined. Changing the geometry from a flat circular plate to a hemispherical or ellipsoidal shell increases the likelihood of a snap-through phenomenon where a sudden jump in deflection may occur from a relatively small increase in force.

In the FE models for ellipsoidal shells, the total load was distributed over a square area (12 inches × 12 inches) to approximate the region of contact produced by a coupler impacting a tank car head. Elastic-plastic material behavior is modeled in the finite element analysis by a piecewise linear representation of the Ramberg-Osgood stress-strain curve, defined by equation (18), for AAR TC-128 tank car steel. The analyses were conducted for shells with clamped edges. Later in this section, the effect of boundary conditions on the load deflection analysis will be examined by considering simply-supported edges. The effects of various geometric, material, and loading parameters on the finite element results will be described in the remainder of this section.

Figure 13 compares the quasi-static FE results for ellipsoidal shells of varying aspect ratios. The FE results for a flat plate (b/a =0) and a hemispherical shell (b/a =1) are plotted in the figure to represent bounding cases. These results correspond to shells or plates with diameter (2a) equal to 87.5 inches and shell thickness (h) equal to 0.5 inches. Initially, the hemispherical shell is stiffer than the flat plate. At a load level of about 100 kips, the load deflection curves for the hemispherical shell and flat plate intersect. For loads greater than 100 kips, the flat plate is stiffer than the hemispherical shell. More-over, the aspect ratio can have a significant effect on the load versus deflection response, especially at force levels greater than 300 kips. Snap-through is most evident in the case of the hemispherical shell where the deflection jumps from about 1.3 to 4.3 inches as the load is increased from 150 to 200 kips. Snap-through also appears to occur in ellipsoidal shells with other aspect ratios, but the magnitude of the deflection and load level at which snap-through occurs decrease as the aspect ratio decreases. At load levels less than 50 kips, the ellipsoidal shells are relatively stiffer than the flat plate. After snap-through occurs, however, the slopes of the load deflection curves for the ellipsoidal shells are less than the slope for the flat plate. The figure also shows the relationship between load and deflection as given by the semi-empirical formula; namely, equation (1). The figure indicates that the semi-empirical equation corresponds approximately to the FE result for an aspect ratio equal to ¼

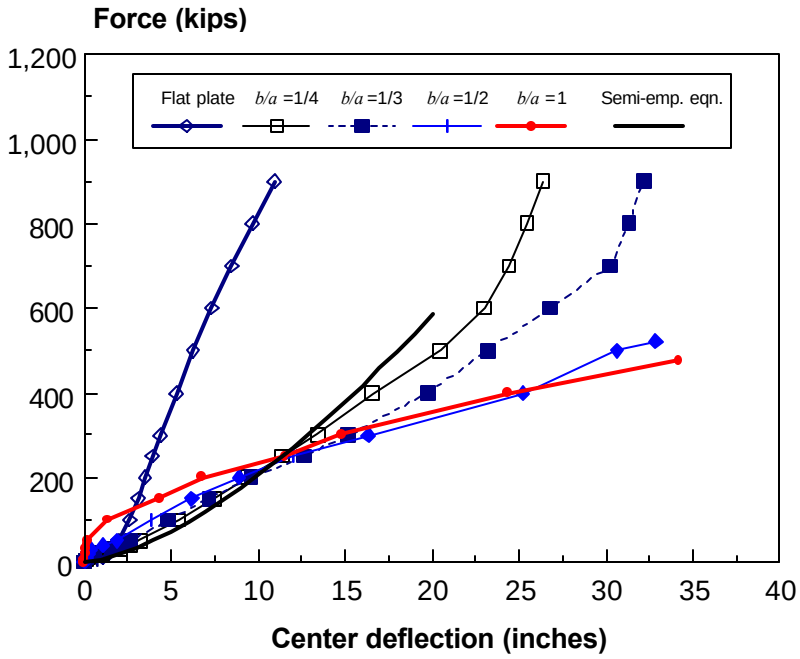

Figure 13. Effect of Aspect Ratio on Elastic-Plastic Finite Element Analysis

The rigid plastic analysis described in Section 3.3.1 assumes that the impact load is applied at the center of the shell. Mathematically, this simplifying assumption reduces a three-dimensional shell-deformation problem to a two-dimensional one. Moreover, this idealization leads to the derivation of closed-form parametric expressions for load and deflection. The finite element method is now adopted to examine the effect of off-center impact loading on the load deflection response of ellipsoidal shells with an aspect ratio of 1/3, tank diameter of 87.5 inches, and shell thickness of 0.5 inch. Figure 14 indicates that off-center loading of the ellipsoidal shell produces a slightly stiffer deflection response compared to the center-loaded case. The difference between the center and off-center loading becomes greater as the load level increases. In this analysis, the off-center load was applied at a distance midway between the center of the tank and its edge. This location corresponds to the height at which full-scale tanks were damaged during simulated coupler-type impact tests (Phillips and Olsen, 1972).

The effect of material properties on the finite element analyses was examined by varying the yield strength in the stress-strain curve with nonlinear strain hardening. In these analyses, the nominal yield strength for tank car steel was assumed to be 50 ksi, and then varied ±30 percent while the modulus of elasticity was held constant at a value of 3×10^7 psi. Figure 15 shows the effect of this variation of yield strength on the load deflection response. The figure indicates that increasing the yield strength produces a stiffer load deflection response.

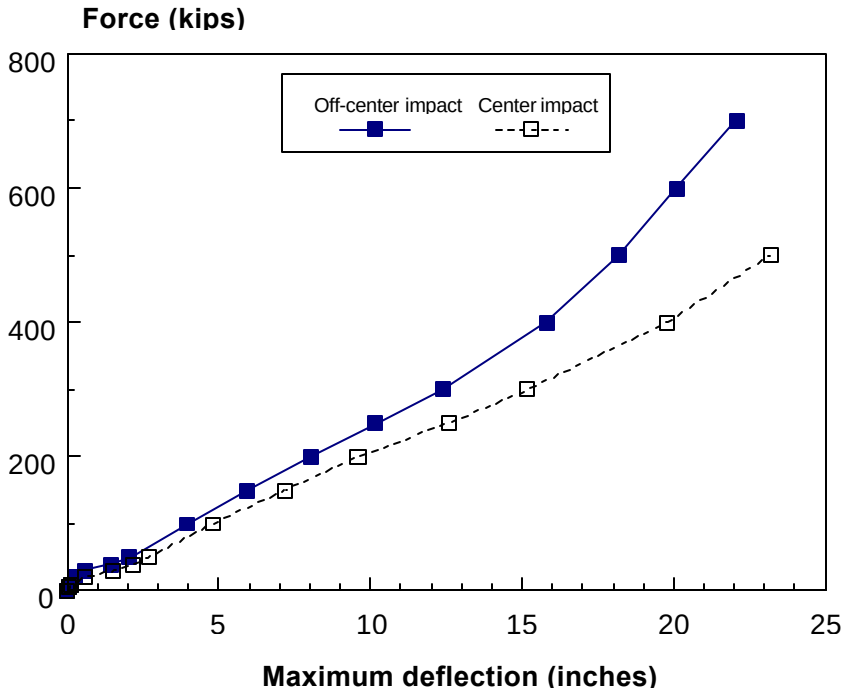

Figure 14. Effect of Off-Center Loading on Elastic-Plastic Finite Element Analysis

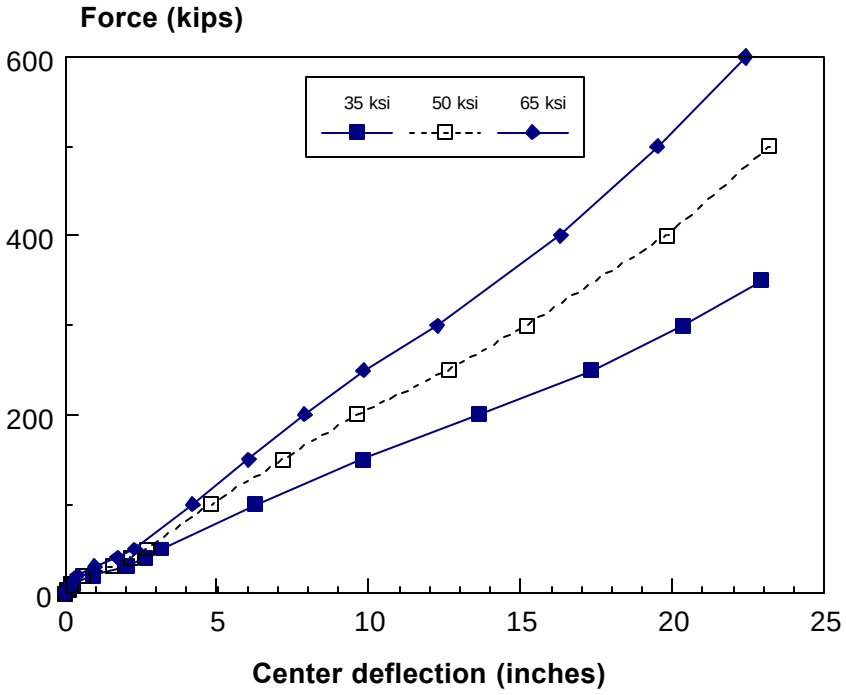

Figure 15. Effect of Yield Strength on Elastic-Plastic Finite Element Analysis

Tank diameter and shell thickness are two additional parameters that define the geometry of the tank car shell. Figure 16 shows the effect of tank diameter on the finite element results. The figure indicates that reducing tank diameter slightly increases the structural stiffness of the shell. The influence of varying the shell thickness is shown in Figure 17. As thickness increases, the structural stiffness of the shell increases. These trends are consistent with the semi-empirical equations. In other words, the finite element method and the semi-empirical approach demonstrate that reducing tank diameter or increasing shell thickness increases the effective structural stiffness of the shell.

Up to this point, the elastic-plastic finite element analyses of ellipsoidal shells were conducted by specifying clamped edges at the boundary conditions. Simply-supported boundary conditions were also considered, and its effect on the FE results is shown in Figure 18. Evidently, the load deflection response is unaffected by boundary conditions for loads are less than 200 kips. For loads greater than 200 kips, the clamped-edge condition produces a stiffer load deflection response than the simply-supported boundary condition.

Figure 19 compares results from the elastic-plastic finite element analysis with the analytical solution for the deflection of rigid plastic ellipsoidal shells. Both analyses were conducted for shells with an aspect ratio of 1/3. Three values for flow stress (20, 35, and 50 ksi) were assumed in the rigid plastic analyses. In the finite element analysis, the load was applied at the center of the shell and was distributed uniformly over a square area equal to 5 percent of the total surface area to approximate a concentrated load. Also, the yield strength and ultimate tensile strength in the elastic-plastic finite element analyses were assumed to be 50 and 81 ksi, respectively. The figure indicates that the results from both the analytical and finite element models have similar trends in the load deflection behavior even though the material characterizations are different. For this reason, the comparison between the finite element and analytical results is considered qualitative. Moreover, the finite element results are bounded by the analytical results for flow stress values between 20 and 50 ksi. These results suggest that representing the tank car head as an ellipsoidal shell with an appropriate choice of a material model can provide a reasonable estimation of its structural behavior.

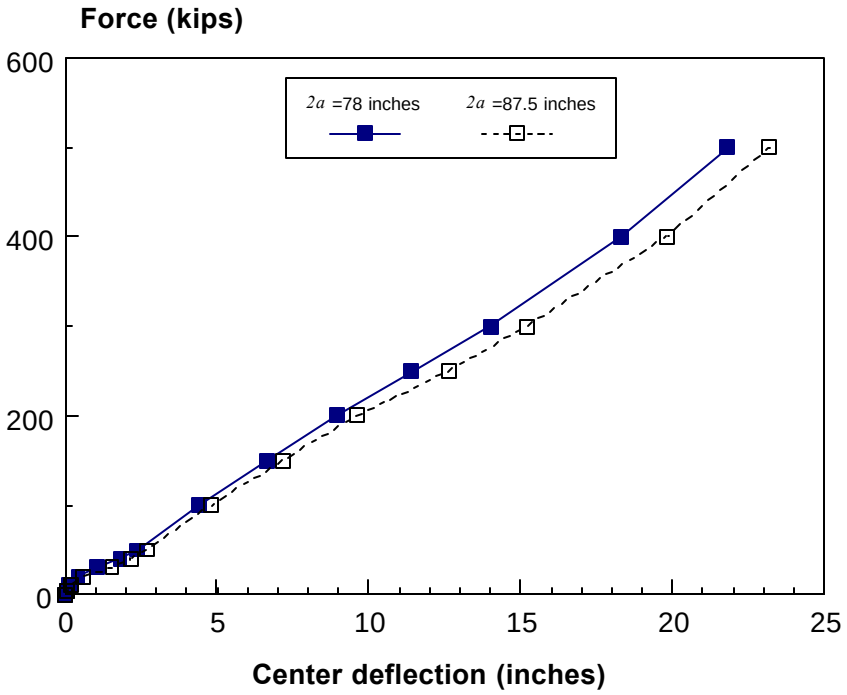

Figure 16. Effect of Tank Diameter on Elastic-Plastic Analysis

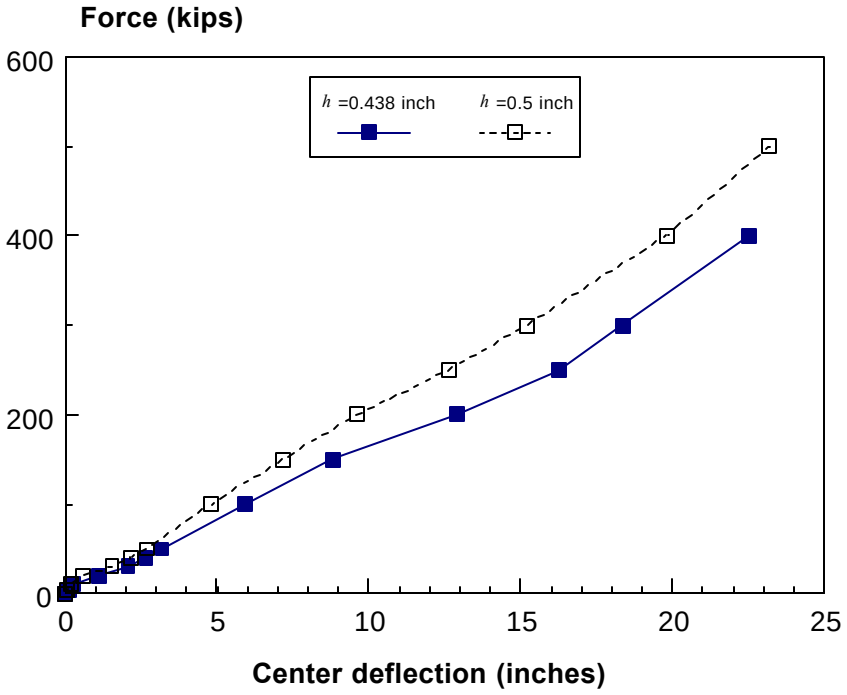

Figure 17. Effect of Shell Thickness on Elastic-Plastic Analysis

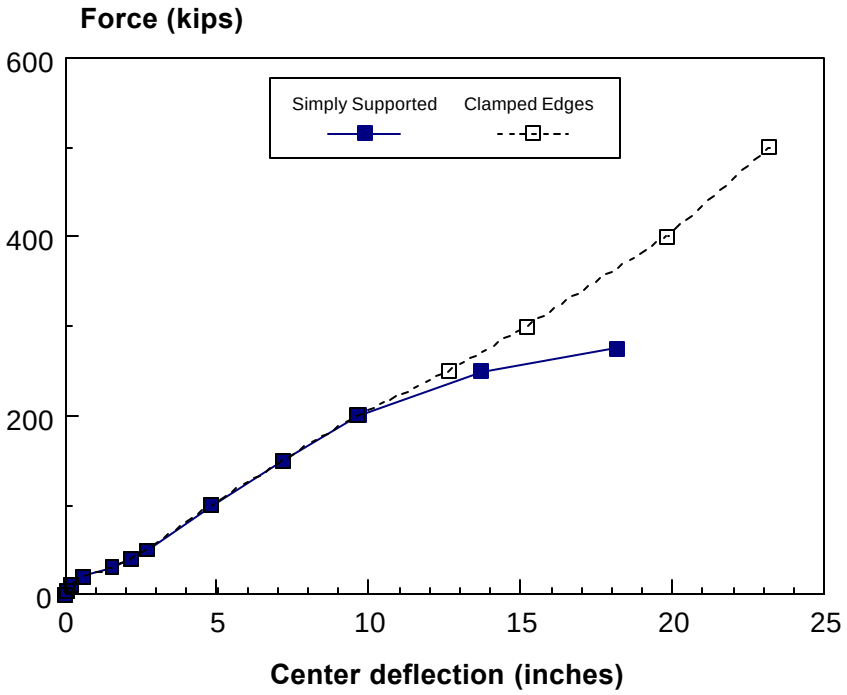

Figure 18. Effect of Boundary Conditions on Elastic-Plastic Analysis

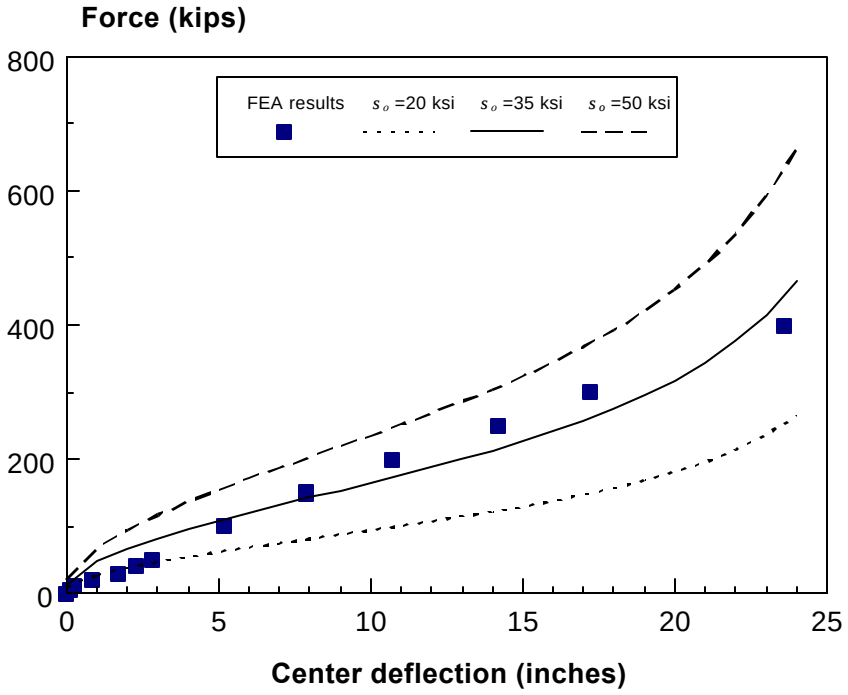

Figure 19. Comparison between Analytical and Finite Element Models

3.2 Impact Force as a Function of Impact Velocity

In order to apply the analyses described in Section 3.1 to tank car impacts, the impact force must be related to the impact velocity. Simple relations can be developed from basic engineering principles to relate the equivalent static force to the impact velocity. However, calculations based on the conservation of energy cannot be realistically applied without estimating the energy lost or absorbed during impact. Also, application of the impulse-momentum principle tends to overestimate the maximum impact force. Moreover, the time duration for the impact event must be assumed when applying the impulse-momentum principle.[2]

Based on limited test data, the load-time history for a coupler impacting the head of a tank car resembles a triangular impulse load with a time duration on the order of 0.25 second. In principle, the peak in the triangular pulse, which represents the maximum impact force, should depend on the impact velocity.

In the present study, a dynamic lumped-mass model was developed which can be used to: (1) determine the load versus time history for a ram car impacting a tank car at a specified impact velocity, and (2) relate the impact velocity to the maximum impact force. The model is shown schematically in Figure 20 where the spring characteristic representing the deformation of the tank car head is assumed to be a nonlinear function of impact load. Moreover, the spring characteristic can be determined from one of the structural analysis models described in Section 3.1.

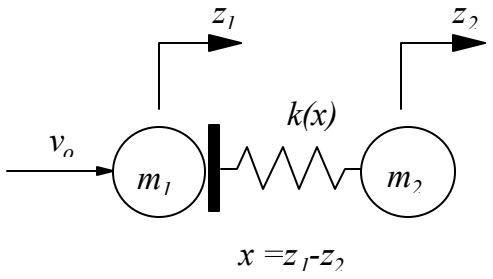

Figure 20. Dynamic Lumped-Mass Model for Tank Car Impact

---

[2] The impulse-momentum principle is expressed mathematically as

$$m_1 v_o = \int_0^t F(t)\,dt$$

where m_1 is the mass of the impacting object, v_o is the initial impact velocity, $F(t)$ is the impact force as a function of time, and t is the impact duration.

For mathematical convenience, the nonlinear spring characteristic in the model is represented by a piecewise linear curve, shown schematically as a hardening spring in Figure 21. Thus, the load versus displacement curve is defined by the coordinates ($ä_i$, F_i) where i is the number of break points in the curve. The piecewise linear representation of the spring characteristic allows for an analytical solution to the equations of motion to the lumped-mass system shown in Figure 20 (for example, refer to Timoshenko, et al., 1974). The mathematical formulation of the dynamic lumped-mass model is described in Appendix B.

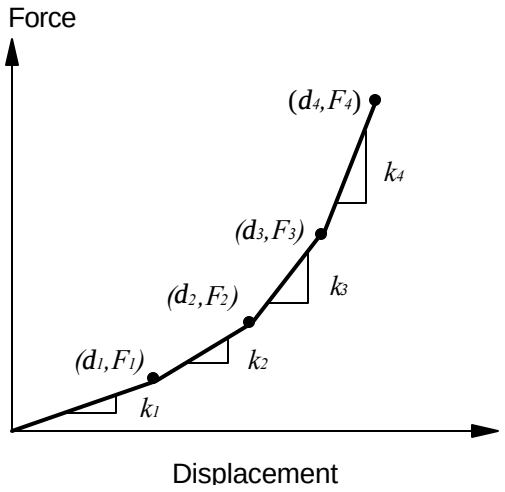

Figure 21. Piecewise Linear Spring Characteristic

Figure 22 shows the force-time histories for four different impact velocities as predicted by the dynamic lumped-mass model. In these results, the spring stiffness in the lumped-mass model was obtained by applying the elastic-plastic finite element model for a centrally loaded ellipsoidal shell with an aspect ratio of ¼, tank diameter of 87.5 inches, and shell thickness of 0.5 inch. The yield strength and the ultimate tensile strength were assumed to be 50 and 81 ksi, respectively, which correspond to the mechanical properties for AAR TC-128 tank car steel. In the dynamic analysis, the ram car weight was equal to 128,900 lb and the reaction-car weight was equal to 48,500 lb. The shapes of the force-time pulse are asymmetrical, and the impact duration varies for different impact velocities. The calculated times for impact duration are on the order of 0.20 second which is slightly less than the observed impact duration time of 0.25 second. Figure 23 shows the variation of peak impact force as a function of impact velocity. The figure also shows the relation between maximum impact force and impact velocity as given by the semi-empirical approach; i.e., equation (5). For this particular structural model, the lumped-mass analysis predicts a larger impact force than the semi-empirical approach at the same velocity.

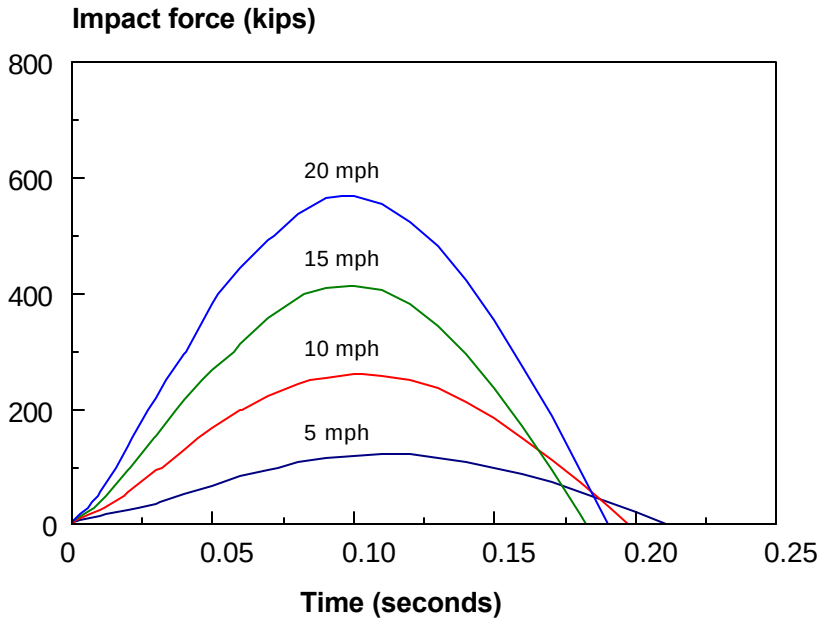

Figure 22. Force Histories for Different Impact Velocities Predicted by Lumped-Mass Model Based on Structural Analysis of an Ellipsoidal Shell

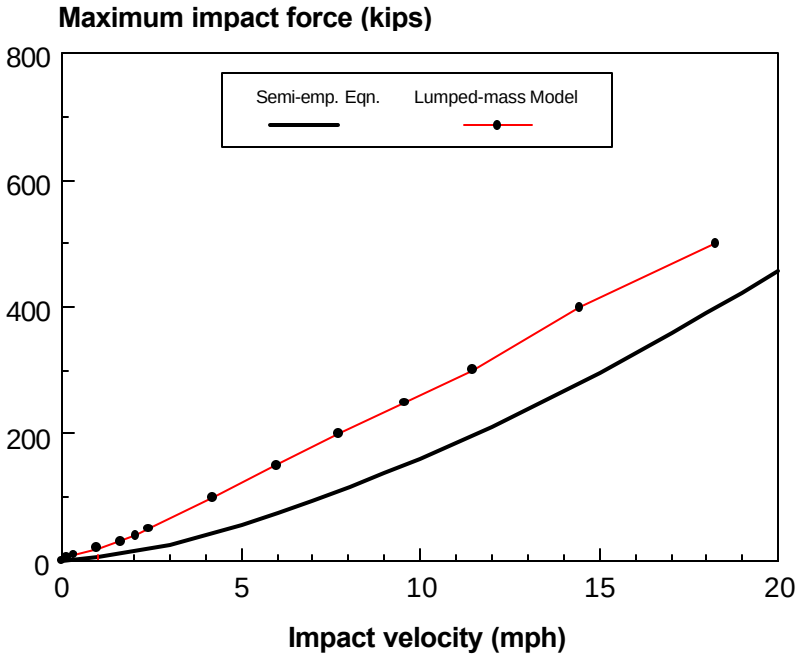

Figure 23 . Comparison between Semi-Empirical Equation and Results from Dynamic Model for an Elastic-Plastic Ellipsoidal Shell

The dynamic lumped-mass analysis was repeated using the same structural model as the previous results, but with the yield strength reduced by 30 percent (i.e., 35 ksi rather than 50 ksi). Figure 24 shows the corresponding force-time histories for varying impact velocities. The impact duration times calculated from the analysis vary between 0.23 and 0.25 seconds, compared to the measured time of 0.25 second. Moreover, the peak impact forces are reduced when a lower yield strength is assumed. Figure 25 shows the variation of the maximum impact force with impact velocity. When compared with Figure 23, these results indicate that a 30 percent reduction in yield strength corresponds to a reduction in peak impact force between 14 and 26 percent depending on the impact velocity. The semi-empirical relation between coupler force and impact velocity is also shown in Figure 25 for comparison. The peak impact force calculated from the engineering analyses is equal to the result from the semi-empirical approach at about 17 mph. Results for impact velocities between 14 and 18 mph are given particular attention because CFR 179.105-5 describes a performance standard requiring tank car heads to withstand minimum impact velocities within this range depending on the ram car weight.

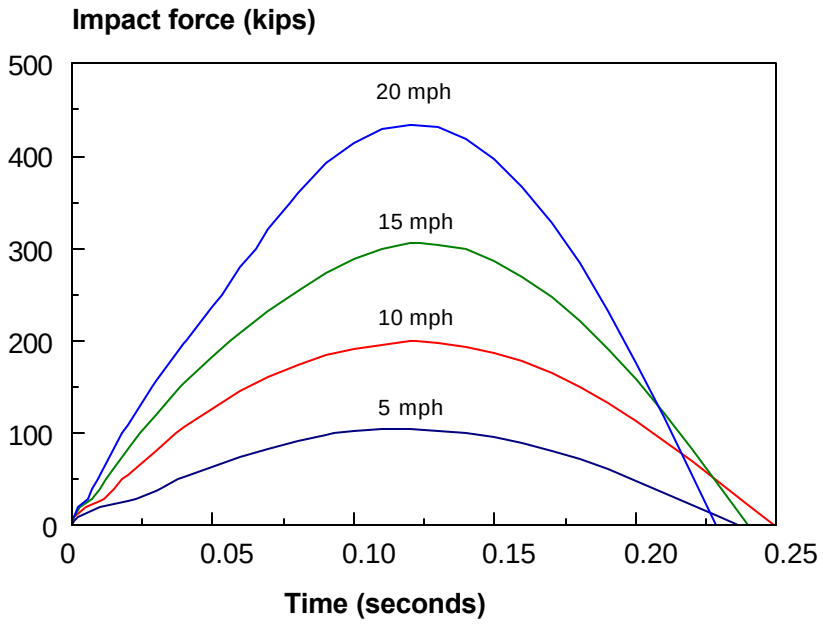

Figure 24. Force Histories for Different Impact Velocities Predicted by Lumped-Mass Model Based on Structural Analysis of an Ellipsoidal Shell

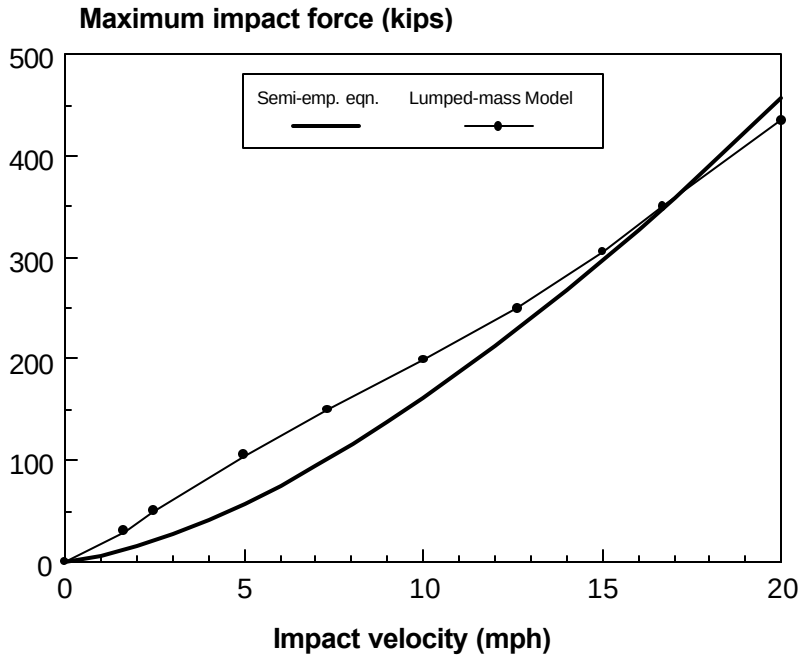

Figure 25. Comparison between Semi-Empirical Equation and Results from Dynamic Model for an Elastic-Plastic Ellipsoidal Shell

3.3 Failure Criteria

In predicting failure, engineering analyses must rely on an appropriate failure criterion. In such analyses, failure (or more specifically, puncture) is assumed to occur when the assumed quantity or criterion (typically, a stress or strain component) exceeds a critical value. In this section, various criteria are examined which can be applied to the structural models described in this report to predict puncture of a tank from impact. These criteria include: (1) transverse shear stress, (2) effective plastic strain, and (3) effective stress.

3.3.1 Transverse Shear Stress

In the semi-empirical approach, the failure criterion was based on the linear elastic solution for the transverse shear stress in a flat circular plate subjected to a centrally applied load:

$$t_{rz} = \frac{3P}{2(2\pi r)h}\left[1-\left(\frac{2z}{h}\right)^2\right] \tag{19}$$

where P is the applied load, r is the radial distance from the center, h is the plate thickness, and z is the transverse co-ordinate through the thickness with its origin at the mid-plane of the plate. From this equation, it can be seen that: (1) the maximum transverse shear occurs at the mid-plane of the plate (i.e., at $z = 0$), and (2) the transverse shear stress has a singularity at the cen-

ter of the plate (i.e., at $r = 0$). Based on linear-elastic plate theory, the transverse shear stress is a linearly increasing function of applied load. Also, this expression is invariant with respect to boundary conditions and the pressure distribution assumed for contact loading. In other words, equation (19) is the same whether the plate is simply supported or has fixed edges, or whether the plate is loaded by a constant uniform load or by a Hertzian distribution over an equal area.

Large deflection finite element analyses were conducted to examine transverse shear for flat circular plates. The finite element analyses, however, calculate a quantity known as the shear resultant which is directly proportional to transverse shear stress. Figure 26 shows the variation of the shear resultant with applied load for different assumptions regarding material behavior. Under nonlinear elastic material behavior, the shear resultant is a monotonically increasing, nonlinear function of applied force. When elastic-plastic material behavior is assumed (represented by a Ramberg-Osgood stress-strain curve in the finite element model), the shear resultant reaches a maximum value at a relatively low load level (on the order of 100 kips). Since the semi-empirical approach is based on Hertzian contact, which is applicable to impact of linear elastic bodies, the use of transverse shear as a failure criterion is consistent with the assumed material model. If, however, an elastic-plastic material model is assumed, these results suggest that using the transverse shear (or equivalently, the shear resultant) as a failure criterion is inappropriate.

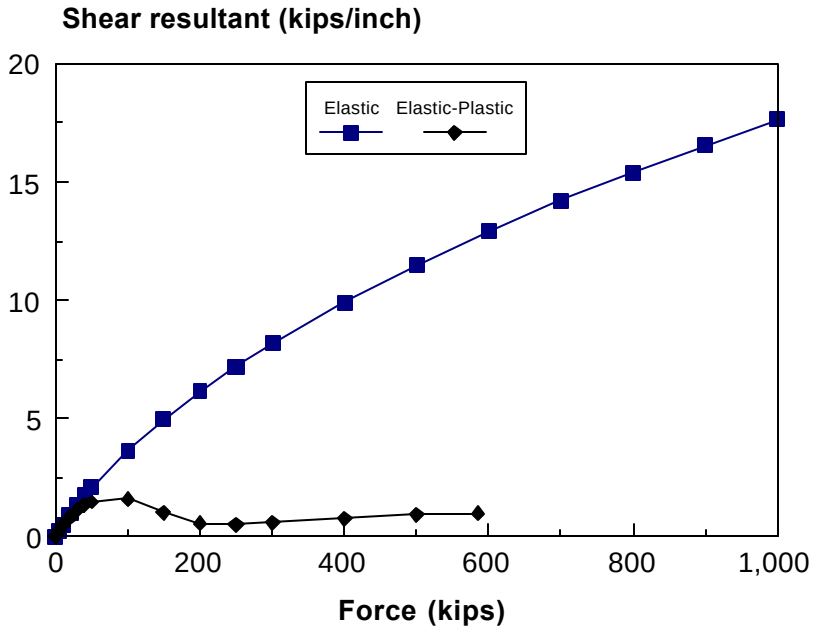

Figure 26. Finite Element Results For Shear Resultant as a Function of Force in Flat Circular Plates

3.3.2 Effective Plastic Strain

The rigid plastic ellipsoidal shell model is used to examine plastic strain as a viable failure criterion for puncture. Referring to Appendix A, the shape of the deformed part of the shell can be described mathematically by:

$$y(x) = y_A + \frac{1}{2Cr}\left[\left(\frac{B}{2}\right)^2 - \left(x - x_B\right)^2\right] \tag{20}$$

from which successive differentiation with respect to x gives:

$$\begin{aligned} \frac{dy}{dx} &= \frac{1}{2Cr}\left(-2x + 2x_A\right) \\ \frac{d^2y}{dx^2} &= -\frac{1}{Cr} \cong \frac{1}{r} \end{aligned} \tag{21}$$

where r is the radius of curvature.

The maximum strain is expected to occur at the plastic-hinge circle, and is defined mathematically as:

$$e_{\max} = \frac{h}{2} \cdot \frac{1}{r} \cong \frac{h}{2} \cdot \frac{1}{Cr} \tag{22}$$

where h is the shell thickness. Also, referring to Appendix A:

$$C = \left(\frac{a}{b}\right)^2 \cos q \tag{23}$$

and

$$r = \frac{1}{2\sin q}\left(\frac{a}{b}\right)\sqrt{3Rh\cos q} \tag{24}$$

where a and b are the semi-major and semi-minor axis lengths of the ellipsoidal shell, respectively. Therefore,

$$e_{\max} = \frac{1}{3}\left(\frac{b}{a}\right)^3 \tan q \sqrt{\frac{3h}{R\cos q}} \tag{25}$$

Strictly speaking, the radius of curvature r is related to the first and second derivatives of y by:

$$\frac{1}{r} = -\frac{y''}{\left[1+(y')^2\right]^{3/2}} \tag{26}$$

The first derivative of y is evaluated at the location of the plastic hinge, or

$$x = x_B = (R-r)\sin\theta \tag{27}$$

Thus,

$$y'(x_B) = \frac{1}{C}\sin\theta = \left(\frac{b}{a}\right)^2 \tan\theta \tag{28}$$

and

$$\varepsilon_{\max} = \frac{1}{3}\frac{\left(\frac{b}{a}\right)^3 \tan\theta}{\left[1+\left(\frac{b}{a}\right)^4 \tan^2\theta\right]^{3/2}} \cdot \sqrt{\frac{3h}{R\cos\theta}} \tag{29}$$

Note, however, that the bracketed term that is raised to the 3/2 power is approximately equal to one for all practical values of *b/a* and è. Therefore, equation (25) is used to calculate the maximum strain.

Figure 27 shows a plot of the maximum strain, as calculated from equation (25), as a function of applied force, as calculated from equation (12), for a variety of cases corresponding to those listed in Table 1. The maximum strain is shown to be a monotonically increasing function of applied load. In each of these cases, the aspect ratio is assumed to be 1/3 and the flow stress is assumed to be 50 ksi. Moreover, failure is assumed to occur when the plastic strain exceeds the ultimate failure strain. For this purpose, a value of 0.2 is assumed as the ultimate failure strain for standard tank car steels. These results indicate that the load at failure varies between 475 and 600 kips depending on the particular case of interest.

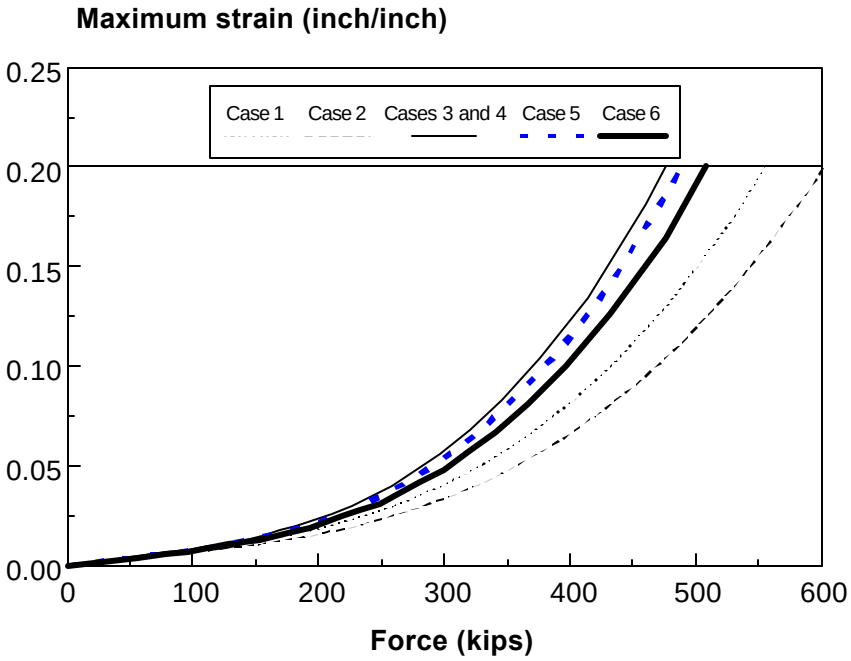

Figure 27. Analytical Results for Maximum Strain as a Function of Force

For comparison purposes, finite element analyses were conducted to calculate the effective plastic strain in elastic-plastic ellipsoidal shells. Figure 28 shows the finite element results in terms of maximum plastic strain as a function of applied load. In these analyses, the aspect ratio was assumed to be ¼. Also, a Ramberg-Osgood stress-strain curve was assumed where the yield strength was equal to 35 ksi. The maximum plastic strain is shown to be a monotonically increasing function of applied force. Assuming failure occurs when the maximum plastic strain is equal to the ultimate failure strain, these results predict that puncture in these cases occurs at load levels between 530 and 590 kips. Moreover, these results suggest that plastic strain is an appropriate failure criterion for elastic-plastic ellipsoidal shells.

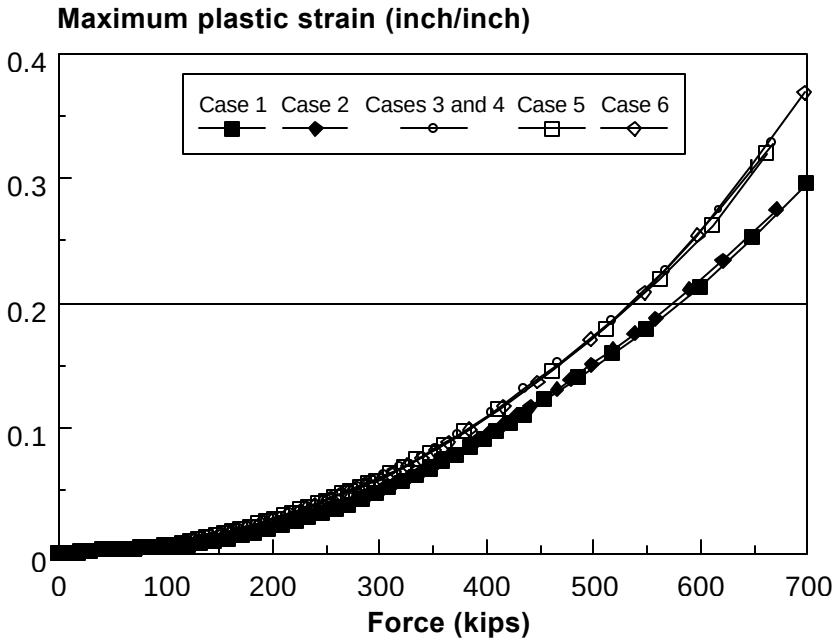

Figure 28. Finite Element Results for Maximum Strain as a Function of Force

3.3.3 Effective Stress

The finite element analyses conducted to examine maximum plastic strain were also used to explore effective stress as a potential failure criterion. Figure 29 shows the finite element results in terms of effective stress as a function of applied load for the various cases. The plots of effective stress correspond to the center of the shell which is where the impact load is applied. The variation of effective stress with applied force somewhat resembles the variation of stress as a function of strain, but with two distinct differences. The first difference is that the effective stress is not a monotonically increasing function of force. The second difference is that the point in these curves that would be analogous to the yield point corresponds to an effective stress of between 55 and 70 ksi at a force level of about 50 kips while the yield strength for this particular material was assumed to be 35 ksi. After yielding has occurred, the effective stress drops off to almost 40 ksi, presumably while the load is redistributed through the shell. At a force level of about 100 kips, the effective stress increases monotonically. A linear extrapolation of these curves shows that an effective stress of 70 ksi would be reached at a force level of about 900 kips. The value of 70 ksi represents the ultimate tensile strength of this particular material. The effective stress does not appear to be an appropriate choice as a failure criterion for elastic-plastic shells mainly because it is not a monotonically increasing function of impact force.

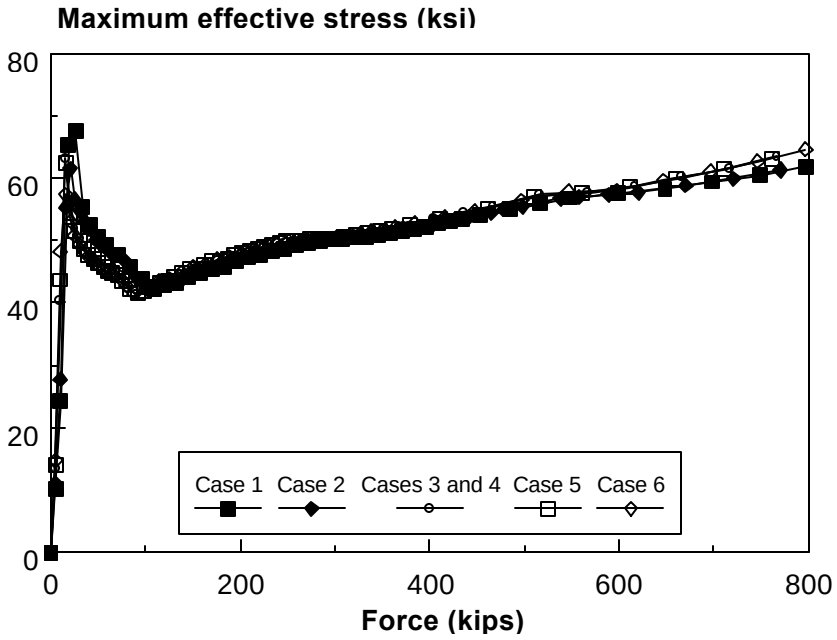

Figure 29. Finite Element Results for Effective Stress as a Function of Force

4. METHODS FOR CALCULATING PUNCTURE VELOCITY

Engineering methods to determine the puncture velocity of tank car shells are described in this section. These methods rely on the engineering analyses described in Section 3. Moreover, the methods are based strictly on engineering mechanics principles and do not include any empiricism. The methods presented here require a structural model to derive a relation between impact force and indentation. The results from the structural model are then applied to the dynamic lumped-mass model to determine the relation between maximum impact force and impact velocity. The results from these two models are combined to estimate the puncture velocity for a given tank car design by assuming an appropriate failure criterion. In this section, two engineering-based methods are presented to determine the puncture velocity of tank car shells. The first approach uses an analytical model for structural analysis of an ellipsoidal shell. The second approach is based on finite element modeling.

4.1 Analytical Method

The first method to calculate puncture velocity is based on the analytical model for a rigid plastic ellipsoidal shell loaded at its apex (Section 3.1.1). The general approach is shown schematically in Figure 30. In the results that follow, the puncture velocity was calculated by assuming maximum strain as a failure criterion. In other words, puncture of the tank car shell is assumed to occur when the maximum strain exceeds a certain critical value. For this purpose, the ultimate failure strain for standard tank car steel (0.2) is assumed as a critical value.

Table 4 compares the puncture velocities estimated by the analytical method with those calculated from the semi-empirical approach. The tank diameter and shell thickness for each case were listed previously in Table 1. Since the specific shape and depth of the tank car head were unknown, three values for aspect ratio were assumed. Also, a flow stress of 35 ksi was assumed in the engineering analysis for each case.[3] Only one full-scale test listed in Table 4 (namely, Case 4) resulted in a puncture of the tank (at an impact velocity of 16.1 mph). Coincidentally, the puncture velocities calculated from the analytical method for an aspect ratio of 1/3 and the semi-empirical approach for this particular case were equal to 15.2 mph. In general, the puncture velocities calculated from the analytical method are less (i.e., more conservative) than those calculated by the semi-empirical approach.

[3] The full-scale impact tests were conducted with tank car heads made from AAR M-115 steel which was reported by Phillips and Olsen (1972) to have a tensile strength between 55 and 65 ksi and a yield strength equal to one-half of the tensile strength.

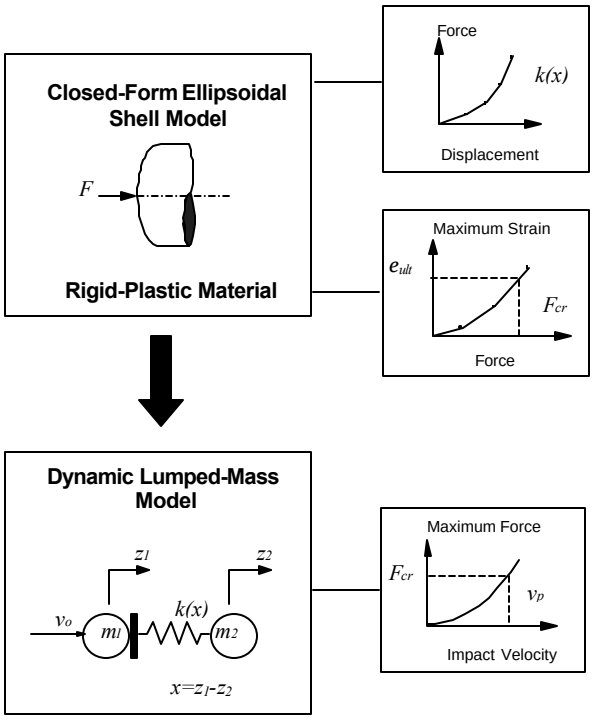

Figure 30. Analytical Method to Calculate Puncture Velocity

Table 4. Puncture Velocities Calculated from Analytical Method for Bare Tank Car Heads

Case	*Outage*	*Puncture Velocity (mph)*			
		Semi-emp. Approach	*Analytical Method*		
			b/a=1/4	*b/a=1/3*	*b/a=1/2*
1	2%	17.9	11.1	12.9	15.8
2	100%	20.1	15.2	17.8	21.9
3	2%	16.5	10.0	11.7	14.5
4	100%	15.2	12.9	15.2	18.7
5	100%	18.0	14.1	16.6	20.5
6	2%	14.6	10.3	12.1	15.0

NOTES:
(1) See Table 1 for structural details corresponding to specific cases.
(2) In the analytical method, the flow stress is assumed to be 35 ksi.

4.2 Finite Element Method

The estimation of puncture velocity based on the analytical solution for ellipsoidal shells is limited to impacts at the center of the tank car head and to rigid plastic material behavior. These limitations can be managed by applying the finite element method but at the expense of more detailed analysis. The application of the finite element method to calculate the puncture velocity of tank cars is shown schematically in Figure 31.

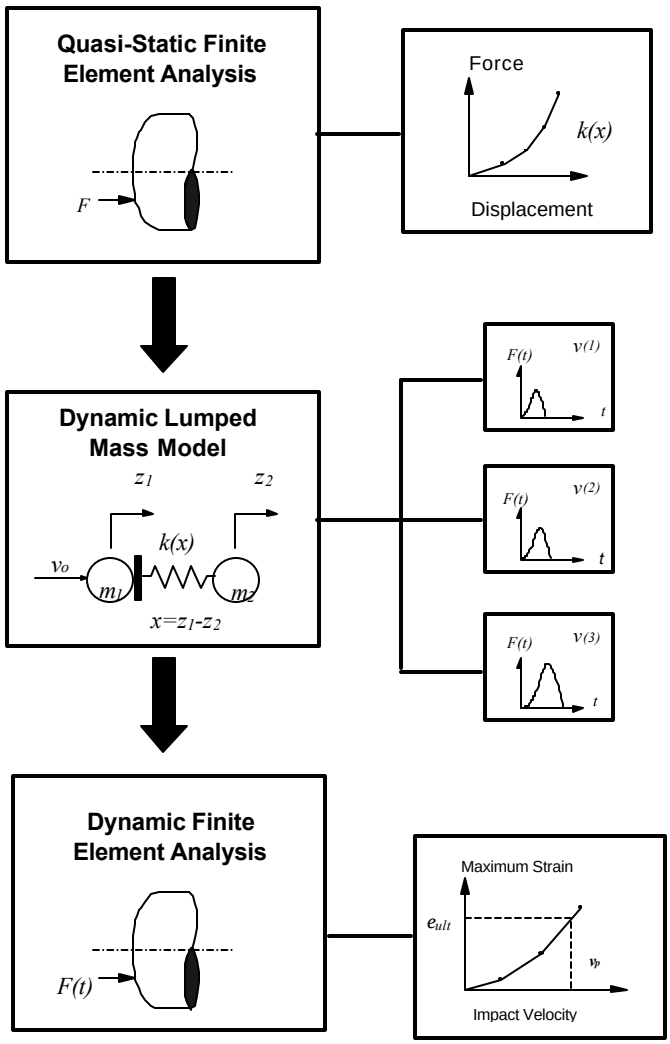

Figure 31. Finite Element Method to Calculate Puncture Velocity

The quasi-static finite element analyses were conducted to determine the load deflection response for the different cases involving bare tank car heads listed in Table 1. In these analyses, the aspect ratio of the tank car head was assumed to be ¼, and the yield strength was assumed to be 35 ksi. Figure 32 shows the load deflection response for the various cases in which the tank diameter and shell thickness are different. The figure also shows the data measured during the tests for indentation and impact force. The two data points at 381 and 410 kips correspond to tests conducted using tanks with 2 percent outage. Otherwise, the general agreement between the finite element analysis and experimental data is reasonable.

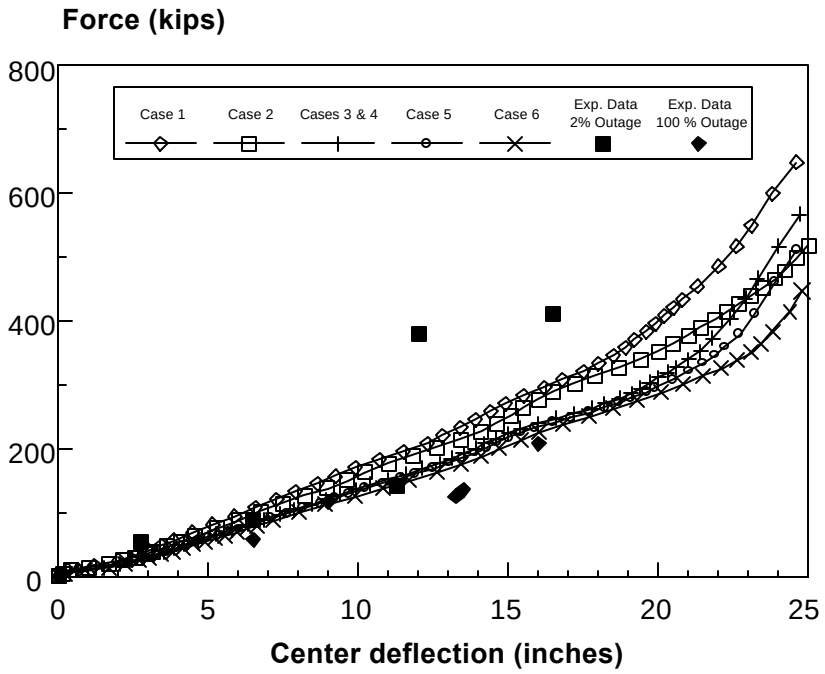

Figure 32. Quasi-Static Finite Element Results for Load deflection Response of Bare Tank Car Heads

The results from the finite element analysis (shown in Figure 32) were used to represent the spring characteristic for the dynamic lumped-mass model to determine the relation between maximum impact force and impact velocity. Results from the dynamic lumped-mass model corresponding to Case 2 are shown in Figure 33. The figure also shows the relationship between maximum force and impact velocity relationship as given by the semi-empirical approach for the same case. The lumped-mass analysis calculates higher maximum force levels than the semi-empirical approach at the same impact velocity.

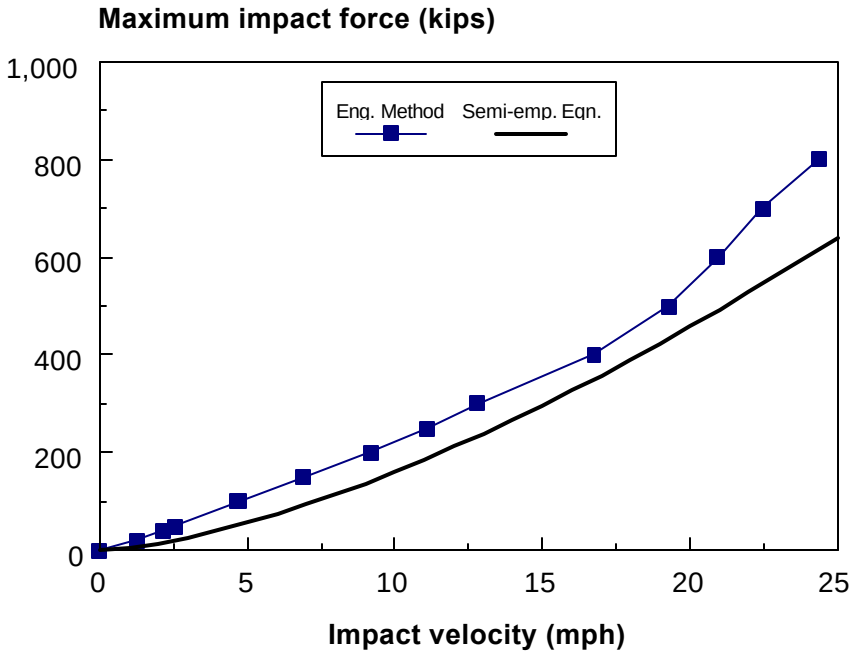

Figure 33. Results from Dynamic-Lumped Mass Analysis for Case 2

In order to predict puncture, the maximum strain was adopted as a failure criterion in the present study. Figure 34 shows the relationship between maximum strain and impact force for Case 2 as determined from the finite element analysis. Failure is expected to occur when the maximum strain reaches 0.2 which corresponds to the ultimate failure strain for tank car steel. Referring to Figure 34, the impact force corresponding to a maximum strain of 0.2 is 577 kips. Referring to Figure 33, a maximum impact force of 577 kips corresponds to an impact velocity of 20.6 mph. In other words, the present methodology calculates a puncture velocity of slightly less than 21 mph for Case 2.

This same procedure can be repeated for the other cases involving bare tank car heads. Table 5 lists the puncture velocities calculated from combining the finite element and lumped-mass analyses with the maximum strain failure criterion. The table also lists the corresponding puncture velocities calculated from applying the semi-empirical approach. In the cases where the outage is 100 percent, the puncture velocities calculated from finite element method are slightly higher than those calculated from the semi-empirical approach. In the cases with 2 percent outage, the trend is reversed; the puncture velocities calculated from the semi-empirical approach are higher than those from the finite element method. In general, the predicted puncture velocities from the present method and the semi-empirical approach are within 20 percent agreement.

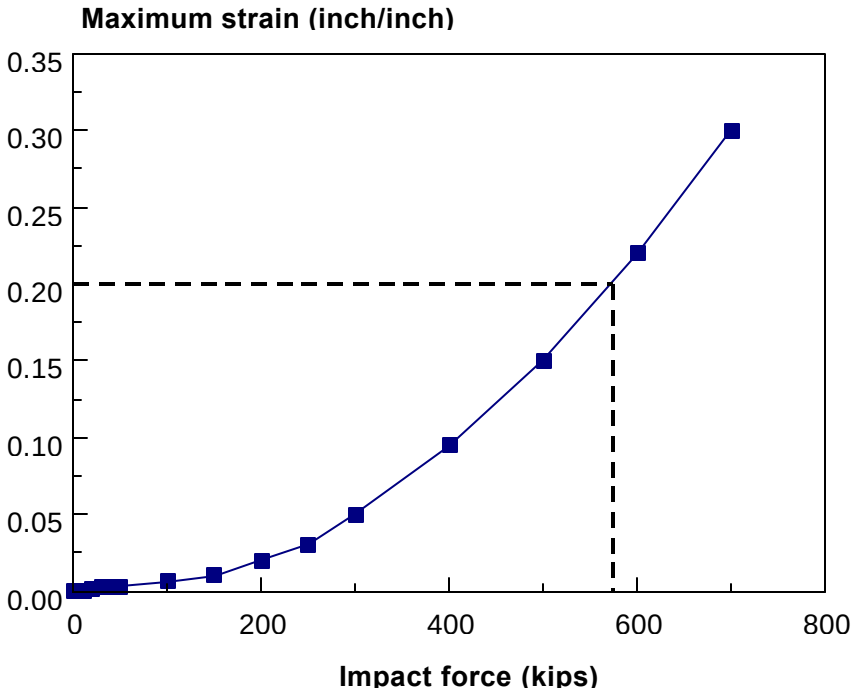

Figure 34. Maximum Strain as a Function of Impact Force for Case 2

Table 5. Puncture Velocities Calculated from Finite Element Method for Bare Tank Car Heads

Case	*Outage*	*Puncture Velocity (mph)*	
		Semi-Empirical Approach	*Finite Element Method*
1	2%	17.9	15.5
2	100%	20.1	20.6
3	2%	16.5	14.0
4	100%	15.2	18.1
5	100%	18.0	19.6
6	2%	14.6	14.0

NOTES:
(1) See Table 1 for structural details corresponding to specific cases.
(2) Aspect ratio is assumed as ¼
(3) Yield strength is assumed as 35 ksi.

In the present study, the NIKE finite element code was used to conduct the quasi-static analyses and the DYNA code was used for the dynamic FEA. Figure 35 compares results of force versus indentation obtained from the NIKE and the DYNA codes. The square symbols represent shells with an aspect ratio of 1/3; the diamonds represent shells with an aspect ratio of ¼ Solid symbols refer to dynamic FE analyses (DYNA), and open symbols refer to the quasi-static FEA (NIKE). The figure shows that the quasi-static and dynamic analyses provide similar results for force versus indentation behavior.

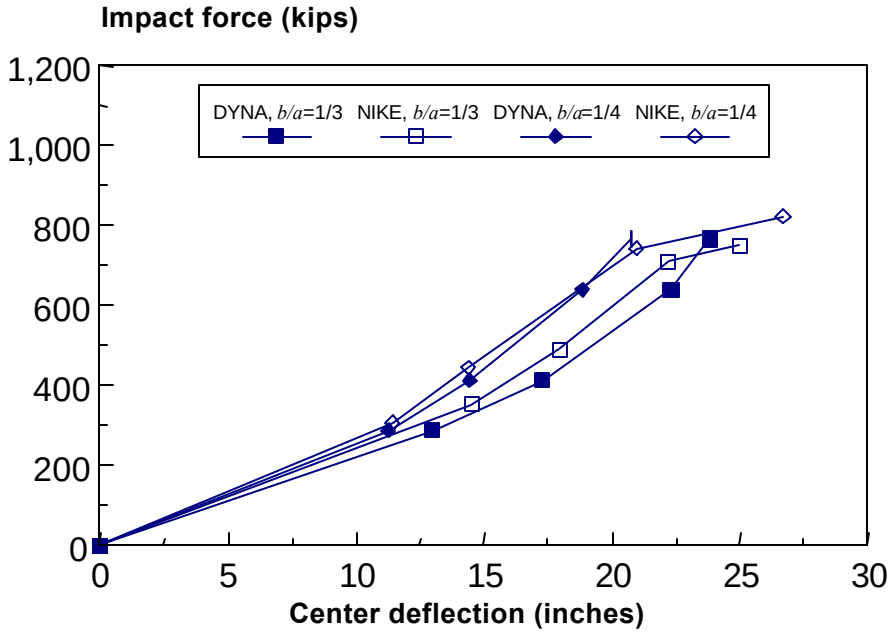

Figure 35. Comparison between Quasi-Static and Dynamic Finite Element Analyses

5. DISCUSSION AND SUMMARY

Engineering analyses were presented in this report that relate impact force and indentation. Specifically, two methods were described: (1) an analytical model of a rigid plastic ellipsoidal shell subjected to a concentrated load at the center, and (2) finite element models of elastic-plastic ellipsoidal shells with arbitrary loading (i.e., load applied at the center or off-center). The effect of various parameters on force-deflection behavior was examined by conducting sensitivity studies on both methods.

Figure 36 illustrates the relative sensitivity of various parameters to indentation at a force level of 500 kips for the rigid plastic shell model. From the semi-empirical equations, 500 kips represents the impact force created from a 128.9-kip ram car colliding with a tank car of equal weight at 20 mph. The baseline parameters are: aspect ratio of 1/3, flow stress equal to 50 ksi, tank diameter equal to 87.5 inches, 0.5-inch shell thickness, and no internal pressure. Thus, the figure shows that for these baseline parameters, the indentation resulting from a 500-kip impact force is 21.2 inches. The figure also shows the range of assumed values for the various parameters that were considered. Based on these results from the analytical model, the various parameters are ranked in order of decreasing sensitivity to load deflection behavior as follows:

- aspect ratio
- internal pressurization
- flow stress
- shell thickness
- tank diameter

In other words, aspect ratio has the strongest influence while tank diameter has the weakest effect on load deflection behavior for this particular model. Internal pressure and flow stress have a strong to moderate effect. Shell thickness has a moderate effect on indentation. The effect of tank diameter on indentation is weak.

Figure 37 is a similar illustration of indentation sensitivity to various parameters considered in the finite element modeling. The baseline value for yield strength in the FE results is 50 ksi. Otherwise, the baseline parameters are identical to those defined for the analytical model. The indentation produced by an impact force of 500 kips, as calculated by the FE analysis for the baseline parameters, is 23.2 inches. Based on the finite element models, the relative ranking of parameters is as follows:

- yield strength
- aspect ratio
- impact load location
- shell thickness
- tank diameter
- boundary conditions

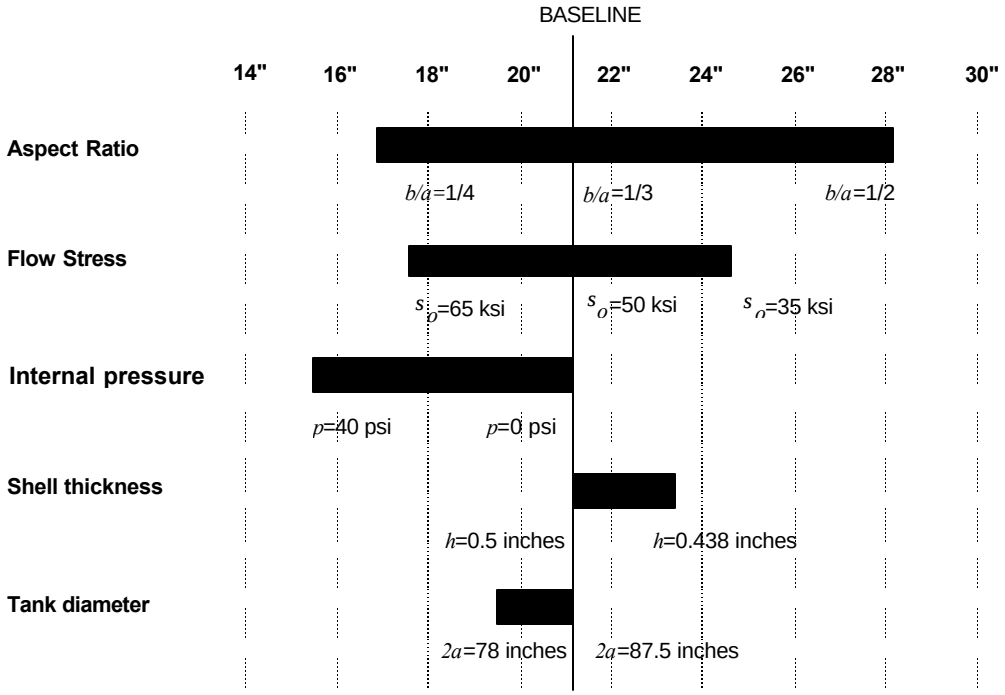

Figure 36. Relative Sensitivities of Various Parameters for Analytical Model (Indentation at an Impact Force of 500 Kips)

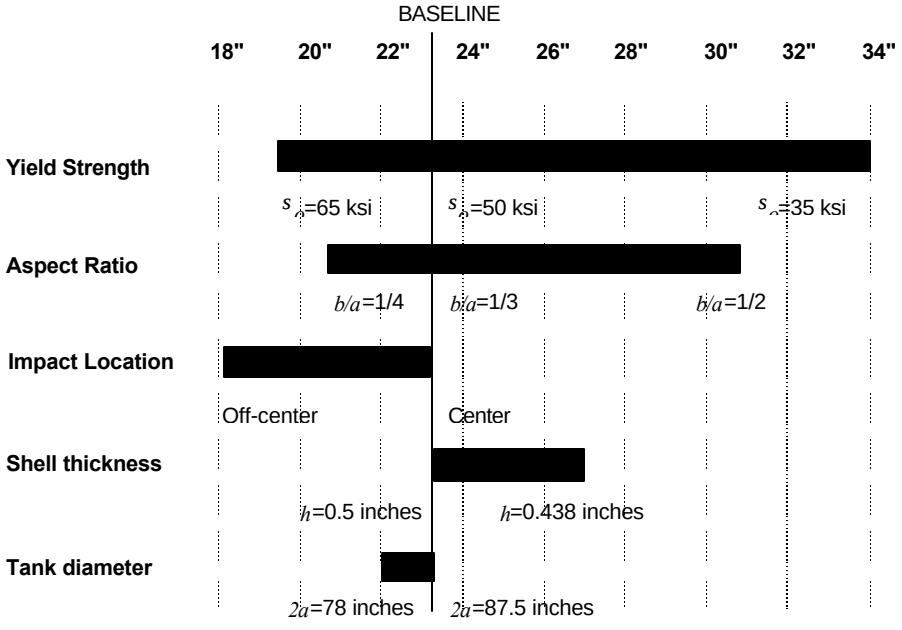

Figure 37. Relative Sensitivities of Various Parameters for Finite Element Model (Indentation at an Impact Force of 500 Kips)

The finite element method confirms the strong sensitivity of indentation to aspect ratio, previously demonstrated in the analytical model. But yield strength is also shown to have a strong influence on indentation. The location of the impact force (off-center versus center impact) and shell thickness have a moderate effect. Tank diameter and boundary conditions have a relatively weak effect on the finite element results for indentation.

Both the analytical and finite element methods indicate that the magnitude of the indentation depends strongly on the shape and depth of the tank car head (i.e., aspect ratio). The semi-empirical approach does not explicitly account for this effect. The methods to determine the puncture velocity of tank cars that are described in this report are based strictly on engineering mechanics principles. No empiricism has been included in these analyses.

Normalization of bare tank car head data indicates that the amount of liquid in the tank (outage) has an influence on the load deflection behavior of tank car heads. While the semi-empirical approach accounts for the effect of internal pressurization, outage is not explicitly taken into account. The effect of internal pressurization on load deflection behavior of ellipsoidal shells was examined using the analytical rigid plastic model. Internal pressure was shown to have less of an effect on the load deflection response than indicated by the semi-empirical approach. Since pressurized tanks generally contain liquid, it appears that the semi-empirical equations overestimate the effect of internal pressurization to compensate for excluding the effect of outage. Future work should be conducted to extend the methods presented in this report to include the effect of outage since it appears to influence structural behavior and, therefore, puncture velocity.

Future work should also be conducted to extend the present methods to include the effect of tank car head protection. For example, the finite element method can be adopted to model concentric ellipsoidal shells to represent a tank car head protected by a head shield. The finite element model would be used to determine the load deflection behavior of such a structure. These results would then be used as input to the dynamic lumped-mass model which would in turn calculate the impulsive force characteristic. Limited test data indicates that the force versus time characteristic for tank heads with head shield protection is trapezoidal in shape. Finite element modeling of this type can be complicated because slip-lines may be needed when the head shield and the tank car head come into contact.

Strain rate effects have not been examined in the present study, but could be incorporated by specifying stress-strain data for varying strain rates into the dynamic finite element model. Such data, however, are limited. Moreover, the effect of strain rate is expected to be small for low velocity impacts.

REFERENCES

Belport, S.M., 1993: "Evaluation of the Puncture Resistance for Stainless Steel and Carbon Steel Tank Heads." AAR Report No. P93-114.

Calladine, C.R., 1983: *Theory of Shell Structures,* Cambridge: London or Cambridge University Press.

Coltman, M., and M. Hazel, 1992: "Chlorine Tank Car Puncture Resistance Evaluation." Final Report, DOT/FRA/ORD-92/11.

de Oliveria, J.G., and T. Weirzbicki, 1982: "Crushing Analysis of Rotationally Symmetric Plastic Shells." *Journal of Strain Analysis for Engineering Design 17*: 229-236.

Jeong, D.Y., Y.H. Tang, and A.B. Perlman, 2001: "Evaluation of Semi-Empirical Analyses for Tank Car Puncture Velocity, Part 1: Correlations with Experimental Data." Draft Final Report.

Larson, W.G., 1992: "Aluminum/Cold Temperature Tank Car Puncture Resistance Tests: Data Report." Final Report, DOT/FRA/ORD-92/29.

Lupker, H.A. 1990: "LPG Rail Tank Car Under Head-On Collision." *International Journal of Impact Engineering 9*: 359-376.

Phillips, E.A., and L. Olsen, 1972: "Final Phase 05 Report on Tank Car Head Study," RPI-AAR Tank Car Safety Research Project, RA-05-17.

Shang, J.C., and J.E. Everett, 1972: "Impact Vulnerability of Tank Car Heads." *Shock and Vibration Bulletin 42,* 197-210.

Timoshenko, S., and S. Woinowsky-Krieger, 1959: *Theory of Plates and Shells,* 2nd Edition, New York: McGraw-Hill Book Company.

Timoshenko, S., D.H. Young, and W. Weaver, Jr., 1974: *Vibration Problems in Engineering,* 4th Edition, New York: John Wiley & Sons.

APPENDIX A. RIGID PLASTIC DEFORMATION OF AN ELLIPSOIDAL SHELL

This appendix presents the derivation of an analytical solution to the rigid plastic deformation of an ellipsoidal shell subjected to a concentrated load applied at the center of the shell. The solution presented in this appendix represents an extension of previous work on the rigid plastic deformation of rotationally symmetric shells of revolution. Specifically, de Oliveira and Wierzbicki (1982) developed an analytical solution for non-pressurized hemispherical shells. Subsequently, Lupker (1990) modified the work of de Oliveira and Wierzbicki to examine the crushing behavior of pressurized hemispherical shells. In the present work the analytical solution is extended to examine the more general case of a pressurized ellipsoidal shell.

The mechanics of the deformation process for rotationally symmetric shells are such that plastic deformations are confined to a narrow zone while the remainder of the shell undergoes rigid body motion. The zone of plastic deformation is characterized as a toroidal surface which moves outward as the applied load increases. In the present formulation, the deformation process for an ellipsoidal shell is assumed to comprise two stages. In the first stage, the deflection at the center of the shell is relatively small (on the order of the shell thickness). Moreover, plastic deformation is contained within a circular area at the center of the shell. As the load level increases, the deformation process progresses to a second stage where the zone of plastic deformation becomes more widespread. In this stage, the plastic deformation is contained within two plastic-hinge circles that move outward from the center as the load increases.

Initial Stage of Deformation Process for an Ellipsoidal Shell

In the initial deformation stage, a small dimple is formed at the center of the ellipsoidal shell where the load is applied. The dimple is bounded by a single plastic-hinge circle. Referring to Figure A1, the radius of the plastic-hinge circle as measured from the vertical axis of revolution is:

$$x_A = R\sin\varphi \tag{A.1}$$

where R is the distance from the origin to the plastic hinge and φ is the angle between R and the y-axis. Physically, the angle φ represents the location of the plastic-hinge circle. For an ellipsoid:

$$R = \sqrt{\frac{a^2 b^2}{a^2\cos^2\varphi + b^2\sin^2\varphi}} \tag{A.2}$$

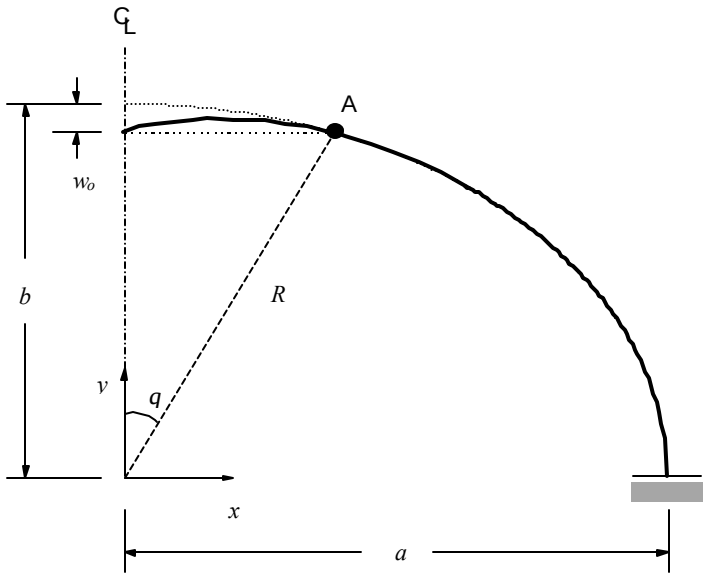

Figure A1. Schematic of Shell Deformation in its Initial Stage

The shape of the undeformed shell is described mathematically as:

$$y_U(x) = b\sqrt{1-\left(\frac{x}{a}\right)^2} \quad for\ 0 \le x \le a \tag{A.3}$$

where a is the semi-major axis length of the ellipsoid and b is the semi-minor axis length. The deformed part of the shell is assumed to have a parabolic shape:

$$y_D(x) = A_0 + A_1 x + A_2 x^2 \quad for\ 0 \le x \le x_A \tag{A.4}$$

where A_0, A_1, and A_2 are unknown constants that are determined by enforcing continuity of slopes and deflections for the undeformed and deformed parts of the shell at the plastic hinge. These continuity conditions are stated mathematically as follows:

$$\begin{aligned} y_U(x_A) &= y_D(x_A) \\ \frac{d}{dx}y_U(x_A) &= \frac{d}{dx}y_D(x_A) \end{aligned} \tag{A.5}$$

where x_A is the location of the plastic-hinge circle, as defined by equation (A.1). Additionally, this formulation assumes that the location of the plastic hinge and the maximum shell deflection relative to the origin are the same, or

$$y_D(0) = y_D(x_A) = R\cos\theta \tag{A.6}$$

After performing the necessary differentiation and algebra,

$$y_D(x) = R\cos\theta + \left(\frac{b}{a}\right)^2 \frac{x}{R\cos\theta}\left[R\sin\theta - x\right] \tag{A.7}$$

The deflection at the center of the shell is:

$$w_0 = b - y_D(0) = b - R\cos\theta \tag{A.8}$$

Second Stage of Deformation Process for an Ellipsoidal Shell.

As the load level increases, the zone of plastic deformation becomes more widespread and moves away from the center. Moreover, two plastic hinges are created during this stage of the deformation process. Also, the zone of plastic deformation is contained within these two plastic-hinge circles which are denoted by Points A and C in Figure A2. Mathematically, the coordinates of these points are defined as follows:

$$\begin{aligned} x_A &= R\sin\theta \\ y_A &= R\cos\theta \end{aligned} \tag{A.9}$$

and

$$\begin{aligned} x_C &= (R-2r)\sin\theta \\ y_C &= y_A = R\cos\theta \end{aligned} \tag{A.10}$$

where r is the radius of the toroidal surface between the hinge points (which is to be determined). In addition, the coordinates:

$$\begin{aligned} x_B &= (R-r)\sin\theta \\ y_B &= (R-r)\cos\theta \end{aligned} \tag{A.11}$$

define the center of the toroid (see Figure A2).

In this stage, the deformed ellipsoidal shell is assumed to consist of two sections. One section is described as the toroidal rise of the shell between plastic-hinge circles. Furthermore, this section of the deformed shell is assumed to have a parabolic shape, which is expressed mathematically as function of x by:

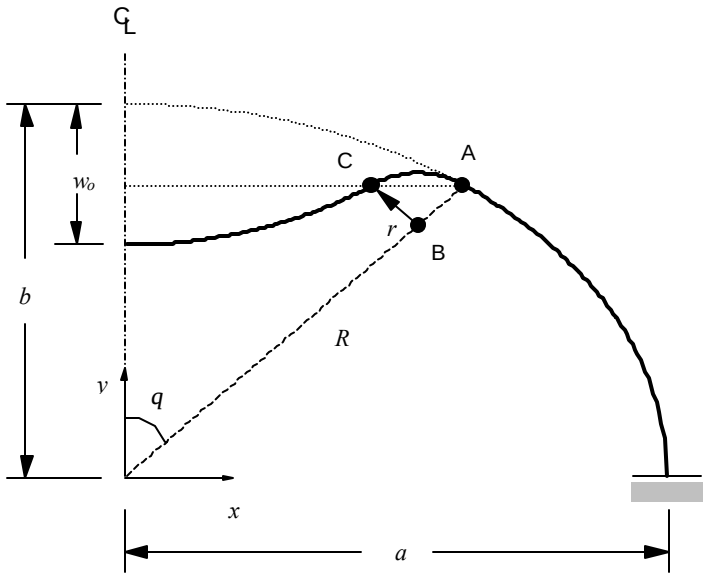

Figure A2. Schematic of Shell Deformation in its Latter Stage

$$y_D^{(1)}(x) = B_0 + B_2\left(x - x_B\right)^2 \quad for\ x_C \le x \le x_A \tag{A.12}$$

where B_0 and B_2 are unknown constants and x_A, x_B, and x_C were defined in equations (A.9), (A.10), and (A.11), respectively. The unknown constants are found by matching the deflections and slopes of the undeformed and deformed shells at Point A. After performing the necessary differentiation and algebra,

$$y_D^{(1)}(x) = R\cos q + \left(\frac{b}{a}\right)^2 \left\{\frac{r^2\sin^2 q - \left[x - (R-r)\sin q\right]^2}{2r\cos q}\right\} \quad for\ x_C \le x \le x_A \tag{A.13}$$

The second part of the deformed shell represents the indentation between the center and the inner plastic-hinge circle. Mathematically, this section is expressed as an ellipse with the same aspect ratio as the undeformed shell but with a different semi-major axis length:

$$y_D^{(2)}(x) = Y_0 - \left(\frac{b}{a}\right)\sqrt{a_2^2 - x^2} \quad for\ 0 \le x \le x_C \tag{A.14}$$

In this equation, Y_0 is the center of the ellipse (representing the inner part of the deformed shell) and a_2 is the length of the semi-major axis for this ellipse. Moreover, this function represents the mirror image of the undeformed shell (which accounts for the negative sign in front of the radical term). The unknown constants, Y_0 and a_2, are determined by enforcing continuity of slopes and deflections of the two functions describing the deformed shell at the inner plastic- hinge circle. These conditions are expressed mathematically as:

$$\frac{d}{dx}y_D^{(1)}(x_C) = \frac{d}{dx}y_D^{(2)}(x_C)$$

$$y_D^{(1)}(x_C) = y_D^{(2)}(x_C) \tag{A.15}$$

From the condition of slope continuity at the inner plastic-hinge circle,

$$a_2 = \left(1 - \frac{2r}{R}\right)a \tag{A.16}$$

From the condition of deflection continuity at Point C,

$$Y_0 = 2(R - r)\cos\theta \tag{A.17}$$

Therefore,

$$y_D^{(2)}(x) = 2(R - r)\cos\theta - b\sqrt{\left(1 - \frac{2r}{R}\right)^2 - \left(\frac{x}{a}\right)^2} \quad for\ 0 \le x \le x_C \tag{A.18}$$

The deflection at the center of the shell is:

$$w_0 = b - y_D(0) = 2\left(1 - \frac{r}{R}\right)(b - R\cos\theta) \tag{A.19}$$

where r is the radius of the toroidal rise of the deformed shell. Moreover, r is determined by minimizing the collapse load which is described in the following section.

Collapse Load

The derivation for the collapse load starts with an energy balance that equates the rate of work of external forces to the internal energy dissipated during the deformation process. The total dissipation energy is the sum of three parts which are due to: (1) a discontinuous velocity field at the plastic-hinge circles, (2) a continuous deformation field in the shell between them, and (3) the work done against internal pressurization. Mathematically, the energy balance is expressed as:

$$\dot{E} = \dot{E}_1 + \dot{E}_2 + \dot{E}_3 \tag{A.20}$$

The rate of work of external loading is given as:

$$\dot{E} = F_o w 2r \sin q \tag{A.21}$$

where F_o is the applied load and w is the angular velocity of the two plastic-hinge circles. The dissipation energy due to the discontinuous velocity field at the plastic hinges contributes:

$$\dot{E}_1 = 2p s_o \frac{h^2}{4} w\left(R \sin q + (R-2r)\sin q\right) \tag{A.22}$$

where s_o is the flow stress and h is the shell thickness. The dissipation energy due to the continuous deformation field between plastic hinges contributes

$$\dot{E}_2 = 2p s_o h w \cdot \left[\frac{1}{3}\left(\frac{b}{a}\right)^2 r \frac{\sin^2 q}{\cos q} \cdot \left(2r \sin q\right)\right] \tag{A.23}$$

where the term in the brackets represents the area of the toroidal rise above the instantaneous center of rotation passing through Points A and C in Figure A.2. The work done against internal pressurization is:

$$\dot{E}_3 = 2p\left\{\int_0^{x_C} p \cdot \dot{w}_1 \cdot x \, dx + \int_{x_C}^{x_A} p \cdot \dot{w}_2 \cdot x \, dx\right\} \tag{A.24}$$

where p is the internal pressure. Also, the deflections rates are:

$$\dot{w}_1 = 2rw \sin q \qquad\qquad \dot{w}_2 = w\left[R \sin q - x\right] \tag{A.25}$$

After substitution and integration,

$$\dot{E}_3 = 2pp\left[\frac{1}{3} r\left(3R^2 - 6Rr + 4r^2\right) w \sin^3 q\right] \tag{A.26}$$

The fully-plastic moment is defined as:

$$M_o = \frac{s_o h^2}{4} \tag{A.27}$$

We also define a dimensionless pressure parameter as:

$$P_o = \frac{pa}{2 s_o h} \tag{A.28}$$

where a is the radius of the tank (which is also the length of the semi-major axis of the undeformed ellipse).

When the equations are combined, the collapse load is found as a parametric function of the angle q :

$$F_o(q) = 2pM_o\left[\frac{4}{3}\frac{r}{h}\left(\frac{b}{a}\right)^2\frac{\sin^2 q}{\cos q}+\frac{R}{r}-1+\frac{4P_o}{ha}\left(R^2-2Rr+\frac{4}{3}r^2\right)\sin^2 q\right] \quad \text{(A.29)}$$

As noted in the previous section, r is an unknown quantity at this point. The procedure to determine r is described as follows. The parametric function for the collapse load, equation (A.29), is differentiated with respect to r. The derivative is set equal to zero. The root of this derivative is the solution for r. A relatively simple closed-form solution for r can be obtained for the case where the internal pressure is zero:

$$r = \frac{1}{2\sin q}\left(\frac{a}{b}\right)\sqrt{3Rh\cos q} \quad \text{(A.30)}$$

In principle, a closed-form solution for r can be obtained for the case of an internally pressurized shell, but the procedure entails the solution of a cubic polynomial in r. In practice, the solution of r for pressurized shells is performed numerically.

Transition Between Deformation Stages

The center deflection in the first stage of the deformation process was determined previously as:

$$w_0 = b - R\cos q \quad \text{(A.8)}$$

Similarly, the center deflection in the latter stage was found to be:

$$w_0 = 2\left(1-\frac{r}{R}\right)\left(b - R\cos q\right) \quad \text{(A.19)}$$

where r was determined by minimizing the collapse load. It is interesting to note that equation (A.19) reduces to equation (A.8) when $R=2r$. Thus, the transition when the deformation progresses from the formation of a single hinge circle to two hinge circles is assumed to occur at the value of q that satisfies this condition. In the case of no internal pressure, the angle at which the transition occurs is found to be a function of the semi-major and semi-minor axis lengths and the shell thickness:

$$q_{trans} = \arccos\left[\frac{\sqrt{2}}{2} b \sqrt{\frac{3ha^2\sqrt{9h^2+4b^2} - 9h^2a^2 - 2b^4}{9h^2a^2(a^2-b^2) - b^6}}\right] \tag{A.31}$$

Mathematically, the initial deformation stage occurs when $q \le q_{trans}$, and the latter stage occurs when $q > q_{trans}$. A similar expression for the transition angle can be found for the case with internal pressurization, but in practice the transition angle is determined numerically.

APPENDIX B. DYNAMIC LUMPED-MASS MODEL FOR TANK CAR HEAD IMPACT

A dynamic lumped-mass model was developed in the present work to determine the force-time history for tank car head impacts. The model is also used to relate the maximum impact force to the initial impact velocity, v_o. As shown in Figure B1, the lumped-mass model comprises two masses representing the impacting car and the tank car and a nonlinear spring between them, representing the stiffness of the tank car head as it deforms during impact.

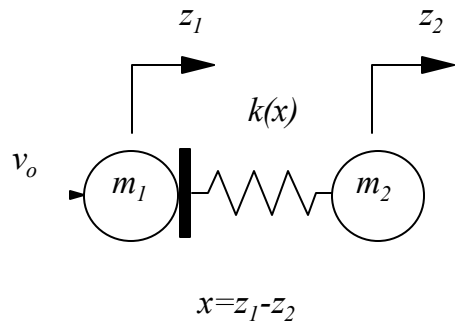

Figure B1. Dynamic Lumped-Mass Model

In the formalism developed in this appendix, the spring characteristic is represented mathematically by a piecewise linear function of impact force, shown schematically in Figure B2 as a hardening spring.

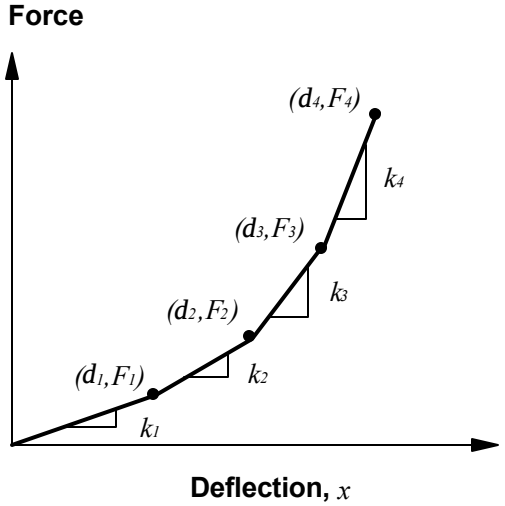

Figure B2. Piecewise Linear Representation Of Spring Characteristic

In the initial linear stiffness range, the equations of motion are:

$$\left.\begin{aligned} m_1\ddot{z}_1^{(1)} + k_1\left[z_1^{(1)} - z_2^{(1)}\right] = 0 \\ m_2\ddot{z}_2^{(1)} + k_1\left[z_2^{(1)} - z_1^{(1)}\right] = 0 \end{aligned}\right\} \quad 0 \le t < t_1 \tag{B.1}$$

where z_1 is the displacement of the ram car which has a mass of m_1, z_2 is the displacement of the reaction or tank car which has a mass of m_2, k_1 is the initial slope of the load-displacement curve, and t_1 is an unknown time to be determined. Also, the superscript refers to the system response in the initial linear regime of the stiffness curve. The general solution to these coupled differential equations in this regime is:

$$\begin{aligned} z_1^{(1)}(t) &= A_1^{(1)} + A_2^{(1)}t + A_3^{(1)}\cos w_1 t + A_4^{(1)}\sin w_1 t \\ z_2^{(1)}(t) &= A_1^{(1)} + A_2^{(1)}t - \frac{1}{a}A_3^{(1)}\cos w_1 t - \frac{1}{a}A_4^{(1)}\sin w_1 t \end{aligned} \tag{B.2}$$

where a is defined as the ratio between the mass of the tank car and the mass of the ram car, or m_2/m_1. Also, the circular frequency of oscillation in this regime is defined as:

$$w_1 = \sqrt{\frac{k_1(m_1+m_2)}{m_1 m_2}} = \sqrt{\frac{k_1(1+a)}{m_1 a}}\,. \tag{B.3}$$

From this equation, the effective mass of the ram car is defined as:

$$m_{eff} = m_1\frac{a}{1+a} \tag{B.4}$$

The four unknown constants in equations (B.2) are determined by applying the following initial conditions:

$$\begin{aligned} z_1^{(1)}(0) &= 0 \\ \dot{z}_1^{(1)}(0) &= v_0 \\ z_2^{(1)}(0) &= 0 \\ \dot{z}_2^{(1)}(0) &= 0 \end{aligned} \tag{B.5}$$

where v_o is the initial impact velocity of the ram car. After applying these initial conditions to the general solution, the motion of the two masses in the initial linear stiffness regime can be expressed in closed-form as:

$$z_1^{(1)}(t) = \frac{v_0}{1+a}\left[t + \frac{a}{w_1}\sin w_1 t\right]$$
$$z_2^{(1)}(t) = \frac{v_0}{1+a}\left[t - \frac{1}{w_1}\sin w_1 t\right] \quad \text{(B.6)}$$

Therefore, the compression of the spring between the two masses is equal to:

$$x^{(1)}(t) = z_1^{(1)}(t) - z_2^{(1)}(t) = \frac{v_o}{w_1}\sin w_1 t\,. \quad \text{(B.7)}$$

At this point, two possible cases must be considered to determine t_1: (1) if the impact velocity v_o is less than $d_1 w_1$, then t_1 is the total time of the impact event; or (2) if the impact velocity v_o is greater than $d_1 w_1$, then plastic deformation of the tank-car head occurs and t_1 is the time when the next break point in the load deflection curve is reached.

In the first case, t_1 is given by:

$$t_1 = \frac{p}{w_1} \quad \text{(B.8)}$$

Moreover, the overall system response in this case is regarded as linear elastic and is therefore, completely described by equations (B.6). Plastic deformations, however, generally occur when the impact velocity is greater than 3 to 4 miles per hour (mph), and t_1 is defined by the second case.

In the second case, t_1 is determined from the following condition:

$$\frac{v_o}{w_1}\sin w_1 t_1 = d_1 \quad \text{(B.9)}$$

Solving this equation for t_1,

$$t_1 = \frac{1}{w_1}\arcsin\left(\frac{w_1 d_1}{v_o}\right) \quad \text{(B.10)}$$

For time after t_1, the stiffness of the tank-car head is governed by k_2 and the relevant equations of motion for this part of the force-deflection curve are:

$$\left.\begin{aligned} m_1\ddot{z}_1^{(2)} + k_2\left[z_1^{(2)} - z_2^{(2)}\right] &= -F_1 + k_2 d_1 \\ m_2\ddot{z}_2^{(2)} + k_2\left[z_2^{(2)} - z_1^{(2)}\right] &= F_1 - k_2 d_1 \end{aligned}\right\} \; t_1 \le t < t_2 \tag{B.11}$$

The general solution to this set of coupled differential equations is similar in mathematical form to the previous case but with complementary terms added to represent the particular solution:

$$\begin{aligned} z_1^{(2)}(t) &= A_1^{(2)} + A_2^{(2)}(t - t_1) + A_3^{(2)}\cos w_2(t - t_1) + A_4^{(2)}\sin w_2(t - t_1) + \frac{1}{2}\left(d_1 - \frac{F_1}{k_2}\right) \\ z_2^{(2)}(t) &= A_1^{(2)} + A_2^{(2)}(t - t_1) - \frac{A_3^{(2)}}{a}\cos w_2(t - t_1) - \frac{A_4^{(2)}}{a}\sin w_2(t - t_1) - \frac{1}{2}\left(d_1 - \frac{F_1}{k_2}\right) \end{aligned} \tag{B.12}$$

where:
$$w_2 = \sqrt{\frac{k_2}{m_{eff}}} \tag{B.13}$$

The unknown constants in equations (B.12) are determined from continuity of displacements and velocities at t_1

$$\begin{aligned} z_1^{(1)}(t_1) &= z_1^{(2)}(t_1) \\ \dot{z}_1^{(1)}(t_1) &= \dot{z}_1^{(2)}(t_1) \\ z_2^{(1)}(t_1) &= z_2^{(2)}(t_1) \\ \dot{z}_2^{(1)}(t_1) &= \dot{z}_2^{(2)}(t_1) \end{aligned} . \tag{B.14}$$

Substituting equations (B.12) into these initial conditions renders:

$$\begin{aligned} A_1^{(2)} &= \frac{1}{1+a}\left[\frac{v_o}{w_1}a\sin\left(\frac{w_1 d_1}{v_o}\right) + \frac{1}{2}(1-a)\left(\frac{F_1}{k_2} - d_1\right)\right] \\ A_2^{(2)} &= \frac{v_o}{1+a} \\ A_3^{(2)} &= \frac{a}{1+a}\cdot\frac{F_1}{k_2} \\ A_4^{(2)} &= \frac{a}{w_2(1+a)}\sqrt{v_o^2 - (w_1 d_2)^2} \end{aligned} \tag{B.15}$$

After the unknown constants in equations (B.12) are determined, two possible cases are considered to determine t_2.

The first case occurs when the initial impact velocity is not high enough for the indentation to reach the next break point in the spring characteristic curve. In this case, t_2 represents the time

when maximum compression of the spring is reached. Mathematically, this condition is satisfied when:

$$\dot{x}^{(2)}(t_2) = \dot{z}_1^{(2)}(t_2) - \dot{z}_2^{(2)}(t_2) = 0 \tag{B.16}$$

After some algebraic manipulations, it can be found that:

$$t_2 = t_1 + \frac{1}{w_2}\arctan\left[\frac{k_2}{F_1 w_2}\sqrt{v_o^2 - (w_1 d_1)^2}\right] \tag{B.17}$$

The second case is when the initial impact velocity is high enough to reach the next break point in the load versus deflection curve. In this case, t_2 is determined from the following condition:

$$x^{(2)}(t_2) = z_1^{(2)}(t_2) - z_2^{(2)}(t_2) = d_2 \qquad \text{(B.18)}$$

After some algebraic manipulations, it can be found that:

$$t_2 = t_1 + \frac{2}{w_2}\arctan\left[\frac{\sqrt{v_o^2 - (w_1 d_1)^2} - \sqrt{v_o^2 - (w_1 d_1)^2 - w_2^2 (d_2 - d_1)\left(2\frac{F_1}{k_2} + d_2 - d_1\right)}}{\left(2\frac{F_1}{k_2} + d_2 - d_1\right) w_2}\right] \tag{B.19}$$

For times after t_2, as defined by equation (B.19), the overall system response requires solution of the following set of coupled differential equations governing the next part of the piecewise linear load deflection curve:

$$\left.\begin{aligned} m_1 \ddot{z}_1^{(3)} + k_3\left[z_1^{(3)} - z_2^{(3)}\right] &= -F_2 + k_3 d_2 \\ m_2 \ddot{z}_2^{(3)} + k_3\left[z_2^{(3)} - z_1^{(3)}\right] &= F_2 - k_3 d_2 \end{aligned}\right\} \quad t_2 \le t < t_3 \tag{B.20}$$

The procedure to solve equations (B.20) is identical to that followed in solving equations (B.1) and (B.11). The general solution to the equations (B.20) is similar to equation (B.12) and also contains four unknown constants:

$$\begin{aligned} z_1^{(3)}(t) &= A_1^{(3)} + A_2^{(3)}(t - t_2) + A_3^{(3)}\cos w_3(t - t_2) + A_4^{(3)}\sin w_3(t - t_2) + \frac{1}{2}\left(d_2 - \frac{F_2}{k_3}\right) \\ z_2^{(3)}(t) &= A_1^{(3)} + A_2^{(3)}(t - t_2) - \frac{A_3^{(3)}}{a}\cos w_3(t - t_2) - \frac{A_4^{(3)}}{a}\sin w_3(t - t_2) - \frac{1}{2}\left(d_2 - \frac{F_2}{k_3}\right) \end{aligned} \tag{B.21}$$

where:
$$w_3 = \sqrt{\frac{k_3}{m_{eff}}} \tag{B.22}$$

The unknown constants are determined from continuity conditions for the displacements and velocities at t_3, from which:

$$\begin{aligned} A_1^{(3)} &= z_1^{(2)}(t_2) + a z_2^{(2)}(t_2) + \frac{1}{2}(1-a)\left(\frac{F_2}{k_3} - d_2\right) \\ A_2^{(3)} &= \dot{z}_1^{(2)}(t_2) + a \dot{z}_2^{(2)}(t_2) \\ A_3^{(3)} &= a \cdot \frac{F_2}{k_3} \\ A_4^{(3)} &= \frac{a}{w_3} \dot{x}^{(2)}(t_2) \end{aligned} \tag{B.23}$$

Subsequently, two possible cases must be considered to determine t_3 which depends on the magnitude of the initial impact velocity. If the initial velocity is not high enough to reach the next break point in the load deflection curve, then:

$$t_3 = t_2 + \frac{1}{w_2} \arctan\left[\frac{k_2}{F_1 w_2}\sqrt{v_o^2 - (w_1 d_1)^2}\right] \tag{B.24}$$

In this case, t_3 represents the time when the maximum spring compression is reached.

The other possible case is when the impact velocity is high enough that the next break point in the load deflection curve is reached:

$$t_3 = t_2 + \frac{2}{w_3} a \tan\left[\frac{\dot{x}^{(2)}(t_2) - \sqrt{\dot{x}^{(2)}(t_2)^2 - w_3^2 (d_3 - d_2)\left(\frac{2F_2}{k_3} + d_3 - d_2\right)}}{\left(\frac{2F_2}{k_3} + d_3 - d_2\right) w_3}\right] \tag{B.25}$$

A pattern in the equations for the system response emerges which can be used to derive successive incremental solutions. Mathematically, the general solution to the i^{th} increment step (for i>2) is:

$$z_1^{(i)}(t) = A_1^{(i)} + A_2^{(i)}(t - t_{i-1}) + A_3^{(i)} \cos w_i (t - t_{i-1}) + A_4^{(i)} \sin w_i (t - t_{i-1}) + \frac{1}{2}\left(d_{i-1} - \frac{F_{i-1}}{k_i}\right)$$
$$z_2^{(i)}(t) = A_1^{(i)} + A_2^{(i)}(t - t_{i-1}) - \frac{A_3^{()}}{a}\cos w_i (t - t_{i-1}) - \frac{A_4^{(i)}}{a}\sin w_i (t - t_{i-1}) - \frac{1}{2}\left(d_{i-1} - \frac{F_{i-1}}{k_i}\right) \quad \text{(B.26)}$$

where:
$$w_i = \sqrt{\frac{k_i}{m_{eff}}} \quad \text{(B.27)}$$

The unknown constants are:

$$\begin{aligned} A_1^{(i)} &= z_1^{(i-1)}(t_{i-1}) + a z_2^{(i-1)}(t_{i-1}) + \frac{1}{2}(1-a)\left(\frac{F_{i-1}}{k_i} - d_{i-1}\right) \\ A_2^{(i)} &= \dot{z}_1^{(i-1)}(t_{i-1}) + a \dot{z}_2^{(i-1)}(t_{i-1}) \\ A_3^{(i)} &= a \cdot \frac{F_{i-1}}{k_i} \\ A_4^{(i)} &= \frac{a}{w_i} \dot{x}^{(i-1)}(t_{i-1}) \end{aligned} \quad \text{(B.28)}$$

When the maximum spring compression is eventually reached, the last incremental solution assumes elastic unloading of the spring along a specified slope k_U. Assuming that t_3, as given by equation (B.24), is the time when the maximum spring compression is reached, the equations of motion for the final incremental solution are:

$$\left.\begin{aligned} m_1 \ddot{z}_1^{(4)} + k_U\left[z_1^{(4)} - z_2^{(4)}\right] &= -F_{\max} + k_U d_{\max} \\ m_2 \ddot{z}_2^{(4)} + k_U\left[z_2^{(4)} - z_1^{(4)}\right] &= F_{\max} - k_U d_{\max} \end{aligned}\right\} \quad t_3 < t \le t_f \quad \text{(B.29)}$$

where t_f is the time for total impact duration which is to be determined. Also,

$$\begin{aligned} d_{\max} &= x^{(3)}(t_3) = z_1^{(3)}(t_3) - z_2^{(3)}(t_3) \\ F_{\max} &= F_2 + k_U\left[x^{(3)}(t_3) - d_2\right] \end{aligned} \quad \text{(B.30)}$$

The general solution to the equations of motion for unloading of the spring is given by:

$$z_1^{(4)}(t) = A_1^{(4)} + A_2^{(4)}(t - t_3) + A_3^{(4)} \cos w_U (t - t_3) + A_4^{(4)} \sin w_U (t - t_3) + \frac{1}{2}\left(d_{\max} - \frac{F_{\max}}{k_U}\right)$$
$$z_2^{(4)}(t) = A_1^{(4)} + A_2^{(4)}(t - t_3) - \frac{A_3^{(4)}}{a}\cos w_U (t - t_3) - \frac{A_4^{(4)}}{a}\sin w_U (t - t_3) - \frac{1}{2}\left(d_{\max} - \frac{F_{\max}}{k_U}\right) \quad \text{(B.31)}$$

where:

$$w_U = \sqrt{\frac{k_U}{m_{eff}}} \tag{B.32}$$

After applying the conditions of continuity of displacements and velocities at t_3, the unknown constants in equation (B.31) are found to be:

$$\begin{aligned} A_1^{(4)} &= z_1^{(3)}(t_3) + a z_2^{(3)}(t_3) + \frac{1}{2}(1-a)\left(\frac{F_{\max}}{k_U} - d_{\max}\right) \\ A_2^{(4)} &= \dot{z}_1^{(3)}(t_3) + a \dot{z}_2^{(3)}(t_3) \\ A_3^{(4)} &= a\,\frac{F_{\max}}{k_U} \\ A_4^{(4)} &= 0 \end{aligned} \tag{B.33}$$

Finally, the total time of the impact, t_f, is determined from the following condition:

$$\ddot{x}^{(4)}(t_f) = 0 \tag{B.34}$$

from which:

$$t_f = t_3 + \frac{p}{2w_U} \tag{B.35}$$